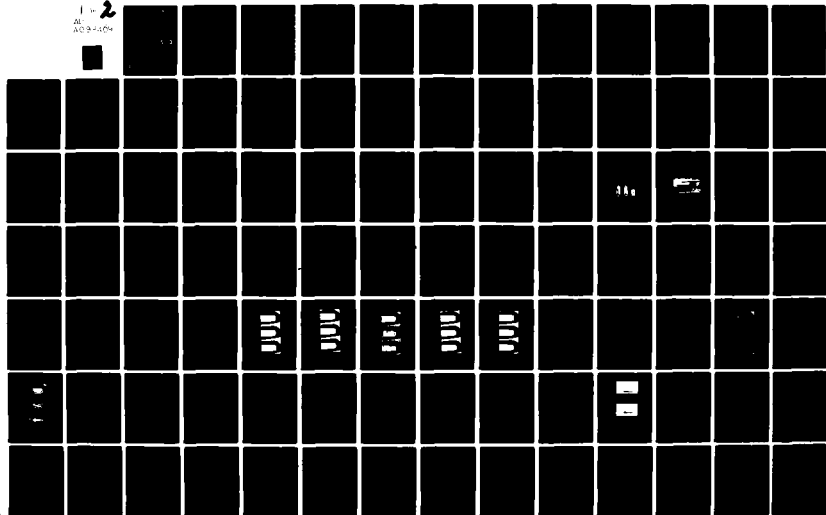


AD-A099 409 PENNSYLVANIA STATE UNIV UNIVERSITY PARK APPLIED RESE--ETC F/G 20/1
TRAVELLING BUBBLE CAVITATION AND RESULTING NOISE.(U)
MAR 81 M F HAMILTON N00024-79-C-6043
UNCLASSIFIED ARL/PSU/TM-81-76 NL

1 - 2
AD-A099-409



⑥ LEVEL II

AD A099 409

TRAVELLING BUBBLE CAVITATION AND RESULTING NOISE

M. F. Hamilton

Technical Memorandum
File No. TM 81-76
2 March 1981
Contract No. N00024-79-C-6043
Copy No. 33

DTIC
ELECTE
S MAY 27 1981 D
B

The Pennsylvania State University
APPLIED RESEARCH LABORATORY
Post Office Box 30
State College, PA 16801

Approved for Public Release
Distribution Unlimited

NAVY DEPARTMENT
NAVAL SEA SYSTEMS COMMAND

DTIC FILE COPY

81 5 26 040

UNCLASSIFIED

SECURITY CLASSIFICATION OF THIS PAGE (When Data Entered)

9; masters thesis

14

ARL/PSU

REPORT DOCUMENTATION PAGE		READ INSTRUCTIONS BEFORE COMPLETING FORM
1. REPORT NUMBER TM-81-76	2. GOVT ACCESSION NO. AD-A099409	3. RECIPIENT'S CATALOG NUMBER
4. TITLE (and Subtitle) TRAVELLING BUBBLE CAVITATION AND RESULTING NOISE.		5. TYPE OF REPORT & PERIOD COVERED MS Thesis, May 1981
7. AUTHOR(s) Mark F. Hamilton		6. PERFORMING ORG. REPORT NUMBER
9. PERFORMING ORGANIZATION NAME AND ADDRESS The Pennsylvania State University Applied Research Laboratory P. O. Box 30, State College, PA 16801		8. CONTRACT OR GRANT NUMBER(s) N00024-79-C-6043
11. CONTROLLING OFFICE NAME AND ADDRESS Naval Sea Systems Command Department of the Navy Washington, DC 20362		10. PROGRAM ELEMENT, PROJECT, TASK AREA & WORK UNIT NUMBERS
14. MONITORING AGENCY NAME & ADDRESS (if different from Controlling Office) 12-137		12. REPORT DATE March 9, 1981
		13. NUMBER OF PAGES 133 pages & figures
		15. SECURITY CLASS. (of this report) Unclassified, Unlimited
		15a. DECLASSIFICATION/DOWNGRADING SCHEDULE
16. DISTRIBUTION STATEMENT (of this Report) Approved for public release, distribution unlimited, per N9SC (Naval Sea Systems Command), 4/13/81		
17. DISTRIBUTION STATEMENT (of the abstract entered in Block 20, if different from Report)		
18. SUPPLEMENTARY NOTES		
19. KEY WORDS (Continue on reverse side if necessary and identify by block number) thesis, bubble, cavitation, noise, theories		
20. ABSTRACT (Continue on reverse side if necessary and identify by block number) Many theories describing cavitation noise model the phenomenon by consider- ing the independent annihilation of cavities in an infinite fluid. Since most practical applications involve cavitation generated by the dynamical action of flow, it is valuable to know how these theories will compare with such experimental data. In this investigation, a Schiebe body is employed as a headform that supports travelling bubble cavitation which is analyzed with regard to the various theories. (cont'd)		

DD FORM 1473 1 JAN 73

EDITION OF 1 NOV 65 IS OBSOLETE
S/N 0102-LF-014-601

UNCLASSIFIED

SECURITY CLASSIFICATION OF THIS PAGE (When Data Entered)

391007

UNCLASSIFIED

SECURITY CLASSIFICATION OF THIS PAGE (When Data Entered)

20. ABSTRACT (continued)

High-speed films were taken of bubbles collapsing on the headform while the accompanying noise signal was recorded. These results showed rebounds to generate almost as much noise as the initial collapse. By counting the number of noise bursts occurring for given noise level and flow parameters, it was found that the noise energy per bubble varies with the cavitation number as roughly σ^{-8} above 10 kHz, but not at all with the free stream flow velocity V_{∞} between 30 and 40 fps. The spectral energy density was observed to be flat, regardless of σ and V_{∞} , from 10 to 100 kHz.

Although maximum bubble radii as functions of σ and V_{∞} were not adequately measured during this study, it is clear that an understanding of this parameter is critical to any cavitation noise theory. The results from this investigation suggest that one might use the linear noise theories for incompressible fluids when analyzing cavitation noise at sufficiently low frequencies. However, it appears that shock wave noise theories are more appropriate for describing the high frequency noise energy.

SECURITY CLASSIFICATION OF THIS PAGE (When Data Entered)

ABSTRACT

Many theories describing cavitation noise model the phenomenon by considering the independent annihilation of cavities in an infinite fluid. Since most practical applications involve cavitation generated by the dynamical action of flow, it is valuable to know how these theories will compare with such experimental data. In this investigation, a Schiebe body is employed as a headform that supports travelling bubble cavitation which is analyzed with regard to the various theories.

High-speed films were taken of bubbles collapsing on the headform while the accompanying noise signal was recorded. These results showed rebounds to generate almost as much noise as the initial collapse. By counting the number of noise bursts occurring for given noise level and flow parameters, it was found that the noise energy per bubble varies with the cavitation number as roughly σ^{-8} above 10 kHz, but not at all with the free stream flow velocity V_∞ between 30 and 40 fps. The spectral energy density was observed to be flat, regardless of σ and V_∞ , from 10 to 100 kHz.

Although maximum bubble radii as functions of σ and V_∞ were not adequately measured during this study, it is clear that an understanding of this parameter is critical to any cavitation noise theory. The results from this investigation suggest that one might use the linear noise theories for incompressible fluids when analyzing cavitation noise at sufficiently low frequencies. However, it appears that shock wave noise theories are more appropriate for describing the high frequency noise energy.

TABLE OF CONTENTS

	<u>Page</u>
ABSTRACT	iii
LIST OF FIGURES	vi
LIST OF TABLES	ix
LIST OF SYMBOLS	x
ACKNOWLEDGMENTS	xii
Chapter	
I. INTRODUCTION	1
1.1 Historical Perspective	1
1.2 Scope of Investigation	4
II. THEORY	6
2.1 Single Bubble Analysis	6
2.2 Scaling Factors	12
III. PROCEDURE	21
3.1 Water Tunnel	21
3.2 Model	21
3.3 Measurement of Test Section Pressure and Velocity	23
3.4 Measurement of Pressure Coefficient	26
3.5 Measurement of Cavitation Inception and Desinence	27
3.6 Air Content	28
3.7 Investigation of Bubble Dynamics	29
3.8 Noise Measurements	34
IV. RESULTS	39
4.1 Pressure Distribution on the Schiebe Body	39
4.2 Cavitation Inception and Desinence	41
4.3 Analysis of Bubble Dynamics	44
4.4 Cavitation Noise	64
V. SUMMARY	90
5.1 Discussion	90
5.2 Conclusion	99

TABLE OF CONTENTS (continued)

	<u>Page</u>
REFERENCES	102
APPENDIX A: Rayleigh Theory of Bubble Collapse	105
APPENDIX B: Acoustic Determination of Inception	107
APPENDIX C: Methods of Counting Cavitation Noise Bursts	110
APPENDIX D: Cavitation Nuclei Analysis Using a Laser Light-Scattering System	117

Accession For	
NTIS GRA&I	<input checked="" type="checkbox"/>
DTIC TAB	<input type="checkbox"/>
Unannounced	<input type="checkbox"/>
Justification	
By	
Distributor/	
Availability Codes	
Dist	Avail and/or Special
A	

LIST OF FIGURES

<u>Figure</u>		<u>Page</u>
1.	Illustration of the 12-Inch Water Tunnel	22
2.	Photograph of the Three Schiebe Bodies Used During the Investigation: (1) Modified with Acoustic Transducers, (2) Unmodified, and (3) Modified with Pressure Taps . . .	24
3.	Photograph of Schiebe Body Mounted in Test Section	25
4.	Schematic Arrangement of High-Speed Photographic Apparatus	30
5.	Illustration Depicting Location of Acoustic Transducer Mounted in Schiebe Body	31
6.	Schematic Diagram Depicting Setup for Recording Cavitation Noise to Accompany the High-Speed Movies . . .	33
7.	Illustration Depicting Location of Hydrophone Used for Measuring Cavitation Noise Level	35
8.	Schematic Diagram Depicting Setup for Recording Cavitation Noise Data	36
9.	Theoretical and Experimental Values of C_p vs. s/a . . .	40
10.	Values of σ_i and σ_d for Travelling Bubble Cavitation, and Values of σ_i for An Attached Cavity, As Functions of V_∞	43
11.	High-Speed Photographs of Cavitation Bubble with $V_\infty = 25$ fps, $\sigma = 0.62$, and Air Content of 4.6 ppm . . .	46
12.	Acoustic Signal and Bubble Volume Plot That Accompany Photographs in Figure 11	51
13.	High-Speed Photographs of Cavitation Bubble with $V_\infty = 25$ fps, $\sigma = 0.68$, and Air Content of 10.0 ppm . . .	54
14.	Acoustic Signal and Bubble Volume Plot That Accompany Photographs in Figure 13	57
15.	Bubble Diameter Plot at $V_\infty = 25$ fps, $\sigma = 0.63$, and Air Content of 4.6 ppm	60

LIST OF FIGURES (continued)

<u>Figure</u>		<u>Page</u>
16.	Bubble Diameter Plot at $V_{\infty} = 25$ fps , $\sigma = 0.86$, and Air Content at 10 ppm	61
17.	Bubble Diameter Plot at $V_{\infty} = 30$ fps , $\sigma = 0.77$, and Air Content at 10 ppm	62
18.	Bubble Diameter Plot at $V_{\infty} = 35$ fps , $\sigma = 0.70$, and Air Content at 10 ppm	63
19.	Hydrophone Beamwidth at Location of Model	65
20.	Response of Hydrophone to (a) 1 Cycle of a 25 kHz Sinusoid, and (b) 16 Cycles of a 25 kHz Sinusoid; Both Generated Adjacent to Model in Test Section	66
21.	Illustration Depicting Direct and Primary Reflection Paths Followed by Sound Generated Adjacent to Model in Test Section	68
22.	Attenuation of Sound by Free Stream Bubbles	70
23.	Example of Cavitation Noise Signal	71
24.	Example of Cavitation Noise Signal	72
25.	Example of Cavitation Noise Signal	73
26.	Noise Burst Interval Distribution	75
27.	Number of Noise Bursts Per Second Versus σ/σ_d at Velocities from $V_{\infty} = 30$ to 40 fps	76
28.	Cavitation Noise Level Versus σ/σ_d at Velocities from $V_{\infty} = 30$ to 40 fps	77
29.	Noise Level Per Bubble Versus σ/σ_d at Velocities from $V_{\infty} = 30$ to 40 fps	78
30.	Noise Level Per Bubble Versus σ at Velocities from $V_{\infty} = 30$ to 40 fps	79
31.	LC-10 Free-Field Transmitting Response	82

LIST OF FIGURES (continued)

<u>Figure</u>		<u>Page</u>
32.	Receiver Response to Omnidirectional White Noise Source Located Adjacent to Model in Test Section	84
33.	Raw Voltage Spectra from Receiver, Uncorrected for Receiver Response to White Noise, of Incipient and Well Developed Travelling Bubble Cavitation at $V_{\infty} = 30$ fps	85
34.	Cavitation Noise Spectrum After Correction for Receiver Response to White Noise, $V_{\infty} = 30$ fps	87
35.	Smoothed Cavitation Noise Spectrum After Correction for Receiver Response to White Noise, $V_{\infty} = 30$ fps	89
36.	Comparison of Experimental Results with Incompressible Theory for Cavitation Noise	92
37.	Schematic Diagram Depicting Setups Used to Count Cavitation Noise Bursts	112
38.	Oscillographs Showing Cavitation Noise and Resulting Output from a Schmitt Trigger for (a) Limited and (b) Developed Travelling Bubble Cavitation	113
39.	Schematic Arrangement of Laser Light-Scattering System . .	118
40.	Oscillograph of Pulses Resulting from Laser Light-Scattering System	119

LIST OF TABLES

<u>Table</u>	<u>Page</u>
1. Equations Defining C Along Surface of Schiebe Body P	42
2. Functional Relationships Deduced for the Dependence of N , L and L_B on σ	80

LIST OF SYMBOLS

a	radius of Schiebe body
c	speed of sound
C_p	pressure coefficient
$C_{p_{min}}$	minimum pressure coefficient
d	distance travelled by bubble with $P < P_v$
f	frequency
k	exponent
L	noise level
L_B	noise level per bubble
M	acoustic Mach number
N	number of noise bursts per second
p	acoustic pressure
P	pressure
P_G	noncondensable gas pressure
P_o	stagnation pressure
P_s	peak shock wave pressure
P_v	vapor pressure
P_∞	free stream static pressure
r	radial coordinate
R	bubble radius
\dot{R}, \ddot{R}	first and second time derivatives of R
R_m	minimum bubble radius
R_M	maximum bubble radius
R_o	initial bubble radius
s	arc length

S	spectral energy density
t	time
T	time period
u	radial velocity
V	bubble volume
\ddot{V}	second time derivative of V
V_{∞}	free stream velocity
θ	time constant
ξ	retarded time
ρ	mass density
σ	cavitation number
σ_d	desinent cavitation number
σ_i	incipient cavitation number
τ	bubble lifetime
τ_c	duration of bubble collapse
τ_g	duration of bubble growth

ACKNOWLEDGMENTS

The entire staff of the Garfield Thomas Water Tunnel is acknowledged for their invaluable assistance to the author during this investigation at that facility. In particular, without the patience and guidance provided by Drs. Donald E. Thompson and Michael L. Billet, the successful completion of this study would not have been realized. Finally, the entire staff of the Hybrid Computer Laboratory at The Pennsylvania State University is gratefully acknowledged for providing the sampling routines used in this study.

This research was supported by the Applied Research Laboratory of The Pennsylvania State University under contract with the United States Naval Sea Systems Command.

CHAPTER I

INTRODUCTION

1.1 Historical Perspective

A fluid may be caused to boil by raising the temperature of the liquid while maintaining a constant pressure, or alternatively, by lowering the pressure while holding the temperature constant. In the latter case, the liquid boils when the pressure falls below the vapor pressure of the fluid. At that point, a phase change occurs spontaneously within the liquid in the form of vapor bubbles. When this pressure drop occurs locally as a consequence of some dynamical action of the flow, the phenomenon is called cavitation (1,2).

Cavitation bubbles, carried by the flow from the low pressure region into a region where the local pressure is again above that of vapor pressure, will collapse as the vapor within the bubble is forced to condense. This collapse can be quite violent, as studies in water have shown the radial velocity of the bubble wall to approach the speed of sound just before annihilation. When this happens, a high amplitude pressure wave, or sound, is caused to propagate away into the medium. As thousands of these collapses may be occurring every second, the total acoustic power being emitted may not only be significant, but a major annoyance.

In order to perform a study of cavitation noise, the manner in which bubbles collapse must be understood. Although it was Besant (3) who, in 1859, first posed the problem of calculating the pressure field caused by the collapse of a spherical cavity in an incompressible fluid,

it was Rayleigh's solution (4) to that problem in 1917 that is regarded as the first conscious application to cavitation. In this idealized problem where the interior of the bubble was assumed to be a void, Rayleigh computed both the collapse time and the surrounding pressure field. However, an unsettling consequence of his analysis was the prediction of an infinite bubble wall velocity as the radius approached zero.

When velocities in fluids approach the speed of sound, it then becomes necessary to include the effects of compressibility. This was not considered until World War II when Kirkwood and Bethe (5) calculated bubble growth resulting from underwater explosions. In 1952, Gilmore (6) extended the Rayleigh analysis to include compressibility using the so-called Kirkwood-Bethe approximation. Mellen (7,8) showed that Gilmore's work predicted bubble wall velocities on the order of the speed of sound, and calculated the resulting shock wave pressure as a function of time. Using spark-induced bubbles, Mellen observed that Rayleigh's theory adequately described the pressure for most of the collapse process, while Gilmore's theory showed the correct trend in the final collapse stage where bubble wall velocities became too large to be described by incompressible theory.

In 1956, Fitzpatrick and Strasberg (9) published a comprehensive survey of cavitation noise. Using the Rayleigh analysis, they showed the acoustic pressure in the far field to be proportional to the second time derivative of the bubble volume. Even more significantly, they predicted a peak in the noise spectrum to occur near a frequency given by the reciprocal of the collapse time that had been derived by

Rayleigh. Data obtained by Mellen (10) was presented in that paper which supported their spectral analysis.

High-speed computers made possible the solution of collapse problems where idealizations could be replaced by suitable parameters. In 1964, Hickling and Plesset (11) performed an excellent numerical analysis of gas-filled bubbles collapsing in a compressible fluid. They showed the important effect that noncondensable gas has on the generation of sound, and its potential to cause the bubble to rebound into another growth stage. For empty cavities, their results proved both Gilmore's collapse velocity and Rayleigh's total collapse time to be remarkably accurate. A similar study conducted by Ivany and Hammitt (12) also included the effects of viscosity and surface tension, but these parameters were shown to have only a minor influence on bubble dynamics.

More recently, Baiter (13), and Esipov and Naugol'nykh (14) derived similar analytical solutions for shock waves emitted by gas-filled bubbles collapsing in incompressible and compressible fluids, respectively. Also, efforts have been made to describe the noise generated by entire cavitating regions as opposed to single bubble analyses. Some of the most promising work in this area has come from the Soviet Union, most notably by Akulichev and Ol'shevskii (15), Il'ichev (16), and Lyamshev (17). A valuable statistical treatment of the conditions under which the single bubble noise theories could be applied to cavitating regions has been provided by Morozov (18). This established an important link between theory and application. Later, Blake et al. (19) performed an experimental investigation to

establish scaling laws for cavitation noise using single bubble analyses. Many other studies have been conducted on noise generated by the interaction of bubbles within flow fields, but these two-phase flow problems are not the subject of this investigation.

1.2 Scope of Investigation

Little has been done experimentally to indicate which theoretical models of cavitation noise are most suitable for application to conditions typically encountered in practice. A number of investigators have studied the collapse and emission of sound by bubbles that were artificially generated by such methods as spark gaps or laser beams (7,20). Since the single bubble noise theories are themselves highly idealized, these experiments provide a valuable basis for comparison. However, the results suggest little concerning situations where parameters related to cavitation caused by liquid flow are involved.

Many experimental investigations have dealt with noise emissions from profusely cavitating regions which are typically generated by sharp edges that disrupt the flow field. This type of cavitation is largely composed of a vaporous froth, and a distinction is made in comparison with limited travelling bubble cavitation where the dynamics of each bubble are considered to be essentially independent of any other bubble. Very often, noise from travelling bubble cavitation is far more intense than that from the foamy variety (19). Also, travelling bubble cavitation lends itself to analysis by the single bubble models of cavitation noise that were previously mentioned, and that is the primary subject of this investigation.

Specifically, the manner in which the noise depends on flow variables such as velocity and pressure is studied. These relationships are of particular interest in developing scaling laws that provide guidelines for extrapolating from test model data to full scale results. A novel approach in this investigation is an analysis of the relationships between cavitation noise and the number of bubbles participating in the phenomenon. Hence, knowledge that can be inferred about how the noise from each single bubble depends on various parameters allows for comparison with a number of theoretical models. In addition, spectra were recorded to show in what frequency regions most of the noise energy is located.

Of course, the total amount of noise from a cavitating region is related to the number of bubbles that are created during cavitation per unit time. In order to predict a priori the intensity of cavitation noise that will occur given certain parameters, it must be known how many bubble collapses can be anticipated. Although an attempt was made to correlate these particular quantitative aspects of cavitation with flow conditions, difficulties in obtaining the necessary data prohibited reaching any reliable conclusions concerning this problem.

CHAPTER II

THEORY

2.1 Single Bubble Analysis

To analyze noise that is generated by limited travelling bubble cavitation, a study is usually made of the dynamics of single bubbles as independent events. This assumption requires that relatively few bubbles coexist in such proximity that they have only a negligible effect on each other. That this condition is met experimentally in this investigation will be shown in a later section.

It is generally considered appropriate to credit Lord Rayleigh with the first explicit analysis of bubble dynamics. His results as published in 1917 (4) were in response to the problem formulated by Besant (3) as follows:

An infinite mass of homogeneous incompressible fluid acted upon by no forces is at rest, and a spherical portion of the fluid is suddenly annihilated; it is required to find the instantaneous alteration of pressure at any point of the mass, and the time in which the cavity will be filled up, the pressure at an infinite distance being supposed to remain constant.

To proceed with Rayleigh's derivation, a number of assumptions must be made. Those that are most important for this study are:

- 1) The liquid is incompressible.
- 2) The pressure and temperature in the interior of the bubble are uniform.
- 3) The bubble and surrounding flow field are spherically symmetrical.
- 4) Body forces are zero.

Following Rayleigh, a spherical bubble of radius $R = R(t)$ having wall velocity $\dot{R} = dR/dt$ is in an incompressible fluid having radial velocity component $u = u(r, t)$ at a distance r from the center of the bubble. From continuity:

$$\dot{R} \cdot 4\pi R^2 = u \cdot 4\pi r^2$$

or

$$u = \left(\frac{R}{r}\right)^2 \cdot \dot{R} \quad (1)$$

The momentum equation for spherically symmetric flow is:

$$-\frac{1}{\rho} \frac{\partial P}{\partial r} = \frac{\partial u}{\partial t} + u \frac{\partial u}{\partial r}, \quad (2)$$

where ρ is the density of the fluid, and $P = P(r, t)$ is the pressure in the fluid at radius r . Now, substituting Equation (1) into Equation (2) results in:

$$-\frac{1}{\rho} \frac{\partial P}{\partial r} = \frac{R^2 \ddot{R} + 2R\dot{R}^2}{r^2} - \frac{2R^4 \dot{R}^2}{r^5},$$

and then integration from R to r leads to:

$$\frac{P(R) - P(r)}{\rho} = -\frac{R^2 \ddot{R} + 2R\dot{R}^2}{r} + \frac{R^4 \dot{R}^2}{2r^4} + R\ddot{R} + \frac{3}{2} \dot{R}^2 \quad (3)$$

Allowing $r \rightarrow \infty$ yields:

$$\frac{P(R) - P(\infty)}{\rho} = R\ddot{R} + \frac{3}{2} \dot{R}^2 \quad (4)$$

Equation (4) is known as the Rayleigh-Plesset equation, and is the nonlinear differential equation that must be solved to determine the radius of the bubble as a function of time. $P(R)$ is the pressure at the bubble wall which, in general, is a complicated function of such parameters as the fluid's vapor pressure, noncondensable gas

pressure, and surface tension and viscous stresses exerted by the fluid. Most significantly, the equation depends upon the environmental pressure that the bubble experiences, $P(\infty, t)$. Hence, one must know the pressure field through which the bubble passes and enter that function into the equation. The Rayleigh-Plesset equation is then solved by numerical techniques.

By relaxing the assumption of an incompressible fluid to allow for the existence of a sound wave, the above equations may be used to predict the acoustic pressure at a distance r due to the motion of the bubble wall. Solving Equation (4) for $P(R)$, substituting that into Equation (3) and rearranging yields:

$$P(r) - P(\infty) = \rho \frac{R^2 \ddot{R} + 2R\dot{R}^2}{r} - \rho \frac{R^4 \dot{R}^2}{2r^4} \quad (5)$$

Since $P(r)$ is the pressure developed at r by the bubble motion, the excess pressure $P(r) - P(\infty)$ may be interpreted as the acoustic pressure $p(r, t)$. At large distances from the bubble, the second term on the right side of Equation (5) may be neglected in comparison to the first term, and the expression can be rewritten (21) as:

$$\begin{aligned} p(r, t) &= \frac{\rho}{r} (R^2 \ddot{R} + 2R\dot{R}^2) \\ &= \frac{\rho}{3r} \frac{d^2(R^3)}{dt^2} \\ &= \frac{\rho}{4\pi r} \ddot{V}(\xi) \quad , \end{aligned} \quad (6)$$

where $\ddot{V} = (4/3)\pi[d^2(R^3)/dt^2]$ is the second time derivative of the bubble volume and $\xi = t - r/c$ is a retarded time incorporating the speed of sound c .

When interpreting Equation (6), one must be aware of the restrictions on the Rayleigh-Plesset equation that must be solved to find $V(t)$. During the final stages of collapse, the inward velocity of the fluid at the bubble wall may exceed the speed of sound, and consequently violate the assumption of an incompressible fluid. In fact, Gilmore (6) modified the Rayleigh-Plesset equation to include the effects of compressibility, and obtained:

$$\frac{P(R) - P(\infty)}{\rho} = R\ddot{R} \left(1 - \frac{\dot{R}}{c}\right) + \frac{3}{2} \dot{R}^2 \left(1 - \frac{\dot{R}}{3c}\right), \quad (7)$$

where c is the speed of sound in the fluid. Notice that, for $\dot{R} \ll c$, Equation (7) reduces to Equation (4).

The solution of Equation (7) shows that the bubble wall velocity does indeed surpass the speed of sound. As a result, a shock wave is generated in the medium. Furthermore, as the bubble wall attains such high velocities, the conditions in the interior of the bubble can no longer be considered quasi-static. This is in violation of the second assumption. Spherical symmetry is also usually violated at that point. Finally, it is not unusual for a small amount of entrained gas to cause the bubble to rebound and commence yet another growth and collapse cycle.

Despite its limitations, the Rayleigh-Plesset equation gives rise to several fairly general predictions concerning bubble dynamics and the associated environmental effects. One particularly simple calculation is of the maximum radius R_M that a bubble is expected to attain due to its passage through a low pressure region. Solutions of the Rayleigh-Plesset equation have indicated that the bubble wall

velocity is relatively constant during most of the growth stage.

Also, the vapor pressure P_v quickly dominates the contribution to the internal pressure $P(R)$ soon after growth has commenced. Hence, solving Equation (4) for \dot{R} after neglecting \dot{R} and substituting P_v for $P(R)$ yields:

$$\dot{R} = \left[\frac{2}{3\rho} (P_v - P) \right]^{1/2}, \quad (8)$$

where $P(\infty)$ has been replaced by P to represent the local pressure that would exist in the absence of the bubble at that particular location.

It is convenient at this point to introduce two commonly used dimensionless expressions for pressure. The pressure coefficient C_p is used in connection with flow around bodies and is defined as:

$$C_p = \frac{P - P_\infty}{\frac{1}{2} \rho V_\infty^2}, \quad (9)$$

where P_∞ and V_∞ are the pressure and velocity, respectively, of the undisturbed flow, and P is the local pressure at the point of interest. Similarly, the cavitation number σ is defined as:

$$\sigma = \frac{P_\infty - P_v}{\frac{1}{2} \rho V_\infty^2}. \quad (10)$$

Substituting both of these quantities into Equation (8) results in:

$$\dot{R} = V_\infty \left[-\frac{1}{3} (C_p + \sigma) \right]^{1/2}. \quad (11)$$

R_M can now be calculated if the time of growth is known. Assuming this time, τ_g , to be the time it takes the bubble to pass through the region where $P < P_v$, then:

$$\tau_g = \frac{d}{v_\infty (1 - \bar{C}_p)^{1/2}}, \quad (12)$$

where d is the distance travelled by the bubble with $P < P_v$, and \bar{C}_p represents the average pressure in that region. Thus, R_M may be approximated by $R_M = \dot{R} \tau_g$, or:

$$R_M = d \left[\frac{\frac{1}{3} \frac{\bar{C}_p + \sigma}{\bar{C}_p - 1}}{\bar{C}_p} \right]^{1/2}. \quad (13)$$

Baiter (13) extends this analysis somewhat to include the inertial effects that contribute to growth after the local pressure has exceeded vapor pressure. This modification is presented as:

$$R_M = d \left[\frac{\frac{1}{3} \frac{\bar{C}_p + \sigma}{\bar{C}_p - 1}}{\bar{C}_p} \right]^{1/2} \left[\frac{\bar{C}_{p1} - \bar{C}_p}{\bar{C}_{p1} + \sigma} \right]^{1/3}, \quad (14)$$

where \bar{C}_{p1} represents the average pressure encountered by the bubble as it enters the high pressure region that will initiate the collapse stage.

If it is further assumed that collapse occurs under the influence of a fairly constant local pressure, as is usually the case, approximate formulas for both the rate of collapse and sound emission may be derived. The Rayleigh analysis is shown in Appendix A to produce the following asymptotic formula for the bubble wall velocity:

$$\dot{R} = v_\infty \left[\frac{1}{3} (C_p + \sigma) \right]^{1/2} \left(\frac{R_M}{R} \right)^{3/2}. \quad (15)$$

Here, C_p represents the local pressure forcing the collapse of a bubble having an initial radius R_M with the condition that $R \ll R_M$.

It can be seen from the formula that the bubble wall is accelerating as it collapses, and consequently, a significant sound wave will be emitted. In fact, the equation indicates that $\dot{R} \rightarrow \infty$ as $(R_M/R)^{3/2}$, or if Gilmore's analysis is used, as $(R_M/R)^{1/2}$. Equation (15) can be solved for R and substituted into Equation (6) to yield:

$$p(r,t) \sim \left(\frac{\rho}{r}\right) v_\infty^{6/5} R_M^{9/5} (C_p + \sigma)^{3/5} t^{-4/5} . \quad (16)$$

Taking the Fourier transform of Equation (16) and squaring the result produces the energy density spectrum of $p(r,t)$:

$$S(f) \sim \left(\frac{\rho}{r}\right)^2 v_\infty^{12/5} R_M^{18/5} (C_p + \sigma)^{6/5} f^{-2/5} , \quad (17)$$

where $S(f)$ describes the energy density at frequency f . Equations (16) and (17) are derived in Appendix A.

The energy roll-off at high frequencies as $f^{-2/5}$ was anticipated by Fitzpatrick and Strasberg (9) in 1956 by using the Rayleigh analysis. They pointed out, though, that the energy must at some point fall off at a higher rate due to the requirement that the pressure pulse have finite energy. It was thought that the problem lies in the fact that linear acoustic theory is incapable of correctly describing the high amplitude, high frequency spike that is part of the pressure pulse.

At low frequencies, Fitzpatrick and Strasberg predicted that the spectrum will increase f^4 . This was concluded by inspection of Equation (6) and knowing that the Fourier transform of the volume $V(t)$, with $V(t)$ nonzero only during the bubble lifetime τ , will be roughly

independent of frequency for $f \ll 1/\tau$. Hence, one then assumes that a maximum in the spectrum will occur at some frequency of the order $1/\tau$.

The previous analysis of bubble dynamics was performed under the assumption of an incompressible medium. However, it seems that the major component of the sound pulse is emitted during the final moments of collapse where the effects of compressibility must be considered. This certainly does not disparage the results of incompressible theory since the sound created by the pertinent stages of collapse is by no means insignificant.

Hickling and Plesset (11) performed extensive numerical analyses of bubbles collapsing in a compressible liquid while taking into account the effects of any noncondensable gas contained in the cavity. For an empty cavity collapsing under the influence of an external pressure between 1 and 10 atmospheres (atm), they predicted that the bubble wall velocity will be asymptotically proportional to $(R_M/R)^{0.785}$. Equation (6) would then predict high frequency energy to fall off as roughly $f^{-4/3}$. They also pointed out that the external pressure does not affect collapse nearly as much as the properties of the gas contained within the bubble.

The presence of gas acts to retard the rate of collapse as the radius goes to zero. This in turn implies an increased attenuation of the high frequency sound components generated during that stage. On the other hand, the gas may cause the bubble to rebound into another growth stage, causing a change in velocity in the surrounding liquid. This change can be propagated through the fluid as a shock wave. Hickling and Plesset noted that the shock wave is most intense at the

initial gas pressures. For example, they showed that an initial gas pressure of 10^{-4} atm will cause a shock front to develop fairly rapidly as a consequence of the high final collapse pressure. As the initial gas pressure is increased, shock formation occurs less quickly until a point is reached where spherical spreading is sufficient to prohibit shock formation altogether. Thus, it seems that appreciable shock formation occurs for only little to no gas content within the bubble.

Equations were derived by Baiter (13) for the acoustic pressure developed by a gas-filled bubble collapsing in an incompressible fluid. His analysis was based upon the Rayleigh-Plesset equation where he let $P(R) = (R_M/R)^4 P_G$ be the internal pressure of the bubble, with P_G the pressure of the noncondensable gases. The development is rather tedious and assumes a priori that a shock wave will be generated having the following form:

$$p(r,t) = P_s e^{-t/\theta} \quad (18)$$

P_s and θ are then given by:

$$P_s = \frac{1}{2} \rho c^2 \frac{R_M}{r} \left(\frac{P_G}{\rho c^2} \right)^{1/4} \left(\ln \frac{r}{R_m} \right)^{-1/2} \quad (19)$$

and

$$\theta = 4.4 \frac{R_M}{c} \left(\frac{P_G}{\rho c^2} \right)^{1/4} \left(\ln \frac{r}{R_m} \right)^{1/2}, \quad (20)$$

where

$$R_m = R_M \left(\frac{3P_G}{P + 3P_G} \right) \quad (21)$$

R_m represents the minimum radius attained by the bubble after its collapse from an initial maximum radius R_M , and again, P is the pressure that would exist in the absence of the bubble at that location.

The above relations assume $P_G \ll P$, $R_m \ll R_M$, and a specific heat ratio equal to 4/3. Note that the magnitude of the shock wave increases with gas pressure, while Hickling and Plesset (11) show the opposite effect for gas pressures above 10^{-3} atm. Since Baiter's analysis required $P_G \ll P$, this suggests $P_G < 10^{-3}$ atm, or just sufficient noncondensable gas pressure to initiate the rebounding action which will generate the shock wave. Increasing that gas pressure beyond 10^{-3} atm will merely serve to cushion the collapse process, and consequently diminish the formation of a shock front.

Esipov and Naugol'nykh (14) performed an analysis of the sound emitted by bubble collapse which took into consideration compressibility as well as noncondensable gas content. Assuming the gas to behave adiabatically with a specific heat ratio again equal to 4/3, and considering the collapse rate to be comparable with the speed of sound, the parameters of a shock wave having the form of Equation (18) were deduced using the Kirkwood-Bethe approximation. These results are similar in form to Equations (19) and (20) with P_s and θ given by:

$$P_s = \frac{1}{\sqrt{2}} \rho c^2 \frac{R_M}{r} \left(\frac{P_G}{\rho c^2} \right)^{1/4} \left(\ln \frac{r}{R_m} \right)^{-1/2} \quad (22)$$

and

$$\theta = \frac{R_M}{c} \left(\frac{P_G}{\rho c^2} \right)^{1/4} \left[M^{-3/2} + 2 \sqrt{2} \left(\ln \frac{r}{R_m} \right)^{1/2} \right] \quad (23)$$

where, in this case, the minimum radius R_m is related to the initial maximum radius R_M by:

$$R_m = R_M M^{-1/2} \left(\frac{P_G}{\rho c^2} \right)^{1/4} \quad (24)$$

and M is an acoustic Mach number that is given by:

$$M = \left[\frac{1}{2} + \frac{3P_G^{3/4} (\rho c^2)^{1/4}}{P} \right]^{-1} \quad (25)$$

The authors emphasized that Equations (22) and (23) may be used only for $P_s \gg \rho c^2/7$ when water is the fluid, and at distances such that $r \gg R_m \exp(M^{3/4})$. Once again, the shock wave seems to become more intense with increasing gas pressure.

An exponential pulse is commonly employed to model the shape of a cavitation shock wave. The energy density spectrum of such a pulse is:

$$S(f) = \frac{(P_s \theta)^2}{1 + (2\pi\theta f)^2} \quad (26)$$

This relation shows the spectrum to be flat at low frequencies and to fall off at high frequencies as f^{-2} . Transition from the low to the high frequency region occurs around $f = 1/2\pi\theta$. Analysis of a shock wave is complicated by the fact that it changes shape while propagating through the medium. For both of the previous analyses, the authors have taken that into account in the derivation of Equation (18). Thus, the implication is that, although the amplitude P_s and the time constant θ will change during shock formation, the pulse will retain its exponential shape and have the same general dependence on frequency.

Of course, cavitation noise does not merely result from the collapse of a single bubble as has been discussed until now, but rather as some particular sequence of events. Consequently, this matter must

be incorporated into any relevant noise theory. For instance, if cavitation is being generated by a source which is periodic in time T , such as a propeller or certain types of turbulent flow, a peak in the noise spectra would be expected to appear at $f = 1/T$. This investigation considers cavitation for which no definite periodicity is anticipated.

Morozov (18) performed a theoretical study of cavitation noise as composed of an aperiodic train of pulses having different amplitudes. A Poisson distribution was chosen to describe the random occurrence of noise pulses. For the special case of identical noise pulses, he found that the noise spectrum was exactly proportional to the spectrum of a single pulse. Even after allowing the noise pulses to have a uniform distribution of size, he concluded that the cavitation noise was still, with reasonable accuracy, correctly modeled by the single bubble theories for a bubble having the same average radius.

2.2 Scaling Factors

Various equations presented in the previous section may be rewritten to illustrate the dependence of a particular variable upon some specific parameter. These are called scaling laws, and are helpful in predicting trends that might be anticipated under certain operating conditions. Conversely, comparing scaling laws with experimental data should suggest whether or not a phenomenon is correctly described by the theoretical model.

The two parameters which are most important in cavitation experiments performed in a closed circuit water tunnel are the free stream velocity V_∞ and pressure P_∞ . Very frequently, trends

depending on pressure are expressed in terms of the cavitation number σ because the vapor pressure P_v can generally be neglected in relation to P_∞ . It must be remembered, though, that σ is itself a function of V_∞ .

Recalling Equation (17), incompressible theory yields a functional relationship for the acoustic energy S of the following form:

$$S(f) \sim V_\infty^{2.4} R_M^{3.6} (C_p + \sigma)^{1.2} f^{0.4} \quad (27)$$

By holding σ constant, and assuming a constant R_M , it is apparent that S should vary as $V_\infty^{2.4}$. The dependence on σ is not as straightforward since R_M is also a function of σ . For instance, either Equation (13) or (14) might be used to describe this dependence. In either case, the lack of a simple power law relating S and σ makes graphical analysis the easiest way to compare the theory with data.

The location of the principal maximum in the energy spectrum was assumed to be near $f = 1/\tau$, where τ is the time required for the bubble to complete its initial growth and collapse cycle. Since it is known that the most significant sound energy is emitted during bubble collapse, it is more realistic to define a new parameter τ_c to represent collapse time. Rayleigh (4) calculated the collapse time of a bubble having initial radius R_M in an incompressible liquid to be:

$$\tau_c \approx 1.3 \frac{R_M}{V_\infty \sqrt{C_p + \sigma}} \quad (28)$$

where $P - P_v$ was taken to be the pressure across the bubble wall.

Hickling and Plesset (11) showed Equation (28) to agree within 1% with their calculations for a compressible liquid when the interior of the bubble was assumed to be a void, i.e., $P_v = 0$. Thus, the maximum in the frequency spectrum might now be expected at $f = 1/\tau_c$ or:

$$f \approx 0.77 \frac{V_\infty}{R_M} \sqrt{C_p + \sigma} \quad (29)$$

Again, Equation (29) is also a complicated function of σ due to its dependence upon R_M .

The two analyses involving shock waves yielded results which are quite similar to each other. In fact, the most significant difference lies in the inclusion of the Mach number in the compressible theory. The value of the Mach number becomes greater than unity for $P_G < 10^{-3}$ atm, and consequently may then be ignored in Equation (23). Furthermore, changes in R_m have only a negligible effect on P_s and θ in both theories due to the logarithmic dependence. Hence, for low noncondensable gas pressures, the compressible theory essentially reduces to the incompressible theory.

Anticipating a high roll-off frequency, it is valuable to see how the theories behave at low frequencies. Recalling Equation (26), it can be seen that the low frequency energy density S may now be determined from $(P_s \theta)^2$, so employing Equations (19) and (20) results in:

$$S(f) \sim R_M^4 P_G \quad (30)$$

Note that the energy density is independent of frequency, and assuming R_M to depend on σ in a manner indicated by Equation (13) or (14) the energy is also essentially independent of the velocity V_∞ with

σ held constant. However, a functional relationship for P_G has not been determined.

Clearly, the maximum bubble radius R_M is an important parameter in all of the theories under discussion, since it merely replaces the initial radius from which bubble collapse begins in each idealized model. Although the equations that describe R_M are very crude indeed, they represent the best available means of calculating this parameter short of solving the Rayleigh-Plesset equation. Both Equations (13) and (14), which were derived under simplified assumptions about bubble dynamics, predict R_M to vary with σ and not with V_∞ . However, data is not yet available that might help show how R_M does vary with V_∞ , and if, in fact, there does exist a significant dependence.

To summarize this section, the scaling laws that have been presented here, in conjunction with the equations for R_M , give an idea of how cavitation noise might vary with pressure and velocity. Although there is still an additional unknown dependence on these flow variables in the form of R_M , these equations will be applied to the data obtained in this investigation to determine which model, if any, provides a suitable description of travelling bubble cavitation noise.

CHAPTER III

PROCEDURE

3.1 Water Tunnel

This experimental investigation of limited travelling bubble cavitation and its resulting noise was conducted at the Garfield Thomas Water Tunnel of the Applied Research Laboratory at The Pennsylvania State University (ARL/PSU). The facility used was a recirculating water tunnel having a 12-inch diameter circular test section in which the flow velocity can be varied continuously to over 70 feet per second (fps). Control of the pressure in the test section was also continuously variable from a minimum of about 3 pounds per square inch (psi) to above 60 psi. This facility is shown schematically in Figure 1.

Clear plexiglass windows mounted in the test section walls had a specific acoustical impedance which was near that of water. The closely matched impedances of the two media results in minimum sound reflection and maximum transmission at the interface formed by the water and the window. One window was carefully designed to be flat on the side in contact with the water, yet not cause cavitation due to its interference with the flow along the cylindrical test section wall. This window was required to reduce optical distortion when a laser or cameras were being used.

3.2 Model

The model used throughout this investigation was a Schiebe nose which is a half-body whose contour is formed by the addition of a disk source to a uniform stream (22). This type of nose does not experience

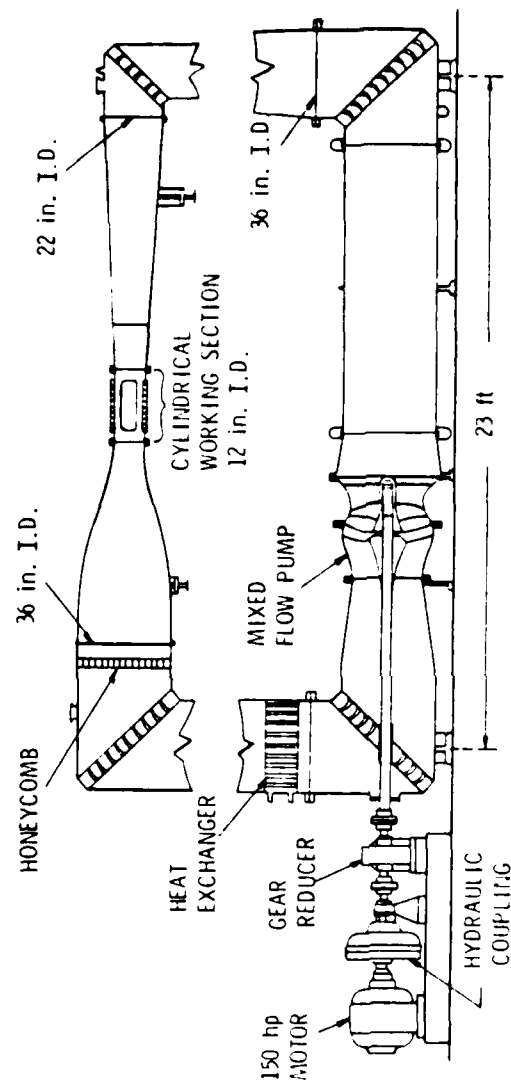


Figure 1. Illustration of the 12-Inch Water Tunnel

laminar separation and supports the type of travelling bubble cavitation that is the subject of this study. Also, the Schiebe body conveniently provides a wide pressure range in which the desired type of cavitation can exist.

A photograph of the three Schiebe bodies used in this study is shown in Figure 2. Each nose has a maximum diameter of two inches and was attached to a downstream tapered afterbody. As pictured in Figure 3, the entire structure was then strut-mounted in the center of the test section.

3.3 Measurement of Test Section Pressure and Velocity

The static and total pressures in the test section were measured using two Bell and Howell static pressure transducers. These transducers were calibrated with a device that consists of a piston attached to a disk on which known weights can be placed. With the disk rotating to reduce friction, various combinations of weights produced suitable pressures within the cylinder for calibrating each transducer. Outputs from the transducers were displayed on integrating digital voltmeters.

Measurement of the static pressure was accomplished by connecting one of the transducers to a tap in the test section wall and comparing that pressure with atmospheric pressure. The velocity was determined by using the other transducer to compare the static pressure in the test section with the stagnation pressure elsewhere along the same streamline. Bernoulli's equation was then employed to solve for the velocity at the point of the static pressure tap.

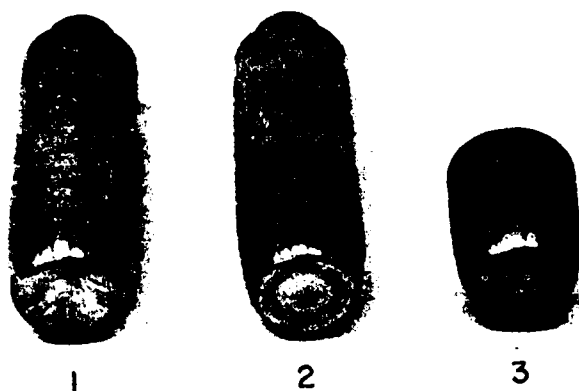


Figure 2. Photograph of the Three Schiebe Bodies Used During the Investigation: (1) Modified with Acoustic Transducers, (2) Unmodified, and (3) Modified with Pressure Taps

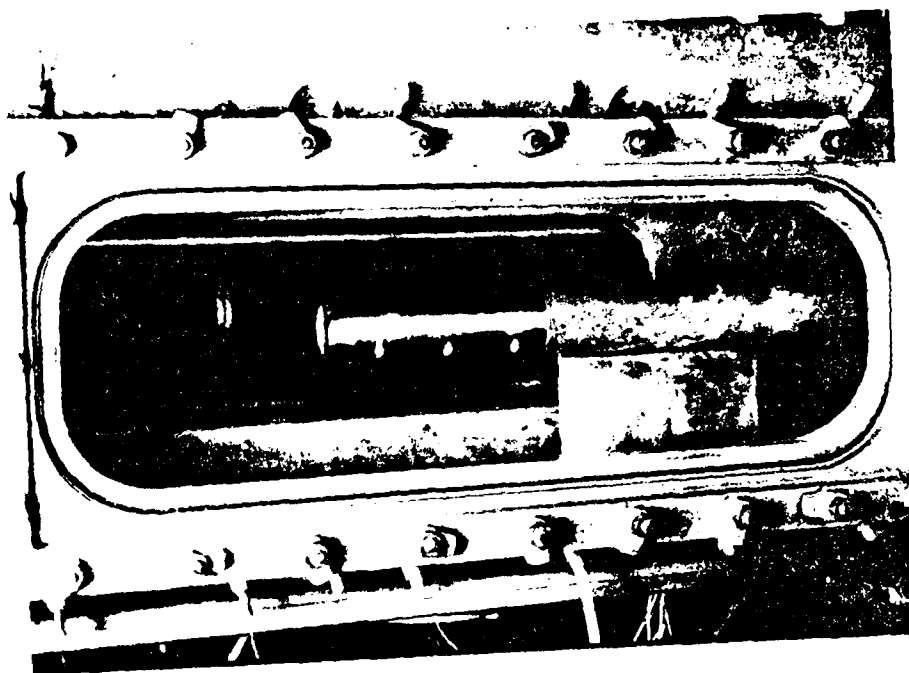


Figure 3. Photograph of Schiebe Body Mounted in Test Section

3.4 Measurement of Pressure Coefficient

An investigation was conducted to determine the pressure distribution along the surface of the Schiebe body. The local pressure at points on the surface of a model is typically expressed using a dimensionless quantity called the pressure coefficient, which was defined in Equation (9). This is repeated here for convenience as:

$$C_p = \frac{P - P_\infty}{\frac{1}{2} \rho V_\infty^2},$$

where P is the local pressure at the point of interest on the body, P_∞ and V_∞ are the respective free stream static pressure and velocity, and ρ is the mass density of the liquid.

The pressure P on the surface of the Schiebe body was measured using a model constructed with ten pressure taps mounted flush with the surface as pictured in Figure 2. A spiral configuration of the taps was chosen so that only the center tap at the stagnation point would lie in the same streamline as any of the other taps. This was an attempt to minimize any flow disturbance at one pressure tap due to another tap upstream.

Each of the ten taps was connected to a scanivalve which coupled any particular tap with a static pressure transducer. The transducer compared this pressure with the free stream static pressure and displayed the difference on a digital voltmeter. The same transducer was used to determine the velocity head by measuring $P_o - P_\infty$, where P_o is the stagnation pressure, and thus, the ratio of the two voltages constituted the dimensionless pressure coefficient. In this manner, values of C_p at each tap were measured six times at each of five different velocities ranging from 20 to 60 fps in increments of 10 fps.

3.5 Measurement of Cavitation Inception and Desinence

The cavitation number σ was defined in Equation (10) and is repeated here as:

$$\sigma = \frac{P_{\infty} - P_v}{\frac{1}{2} \rho V_{\infty}^2},$$

where P_{∞} and V_{∞} are the respective free stream static pressure and velocity, ρ is the mass density of the liquid, and P_v is the vapor pressure. For a given temperature, ρ and P_v will remain constant. Thus, for a constant flow velocity, σ depends only on the free stream static pressure.

As the pressure is lowered at a particular velocity, the point at which cavitation on the model is first observed is called cavitation inception and is denoted by σ_i . Similarly, the point at which cavitation disappears when raising the pressure marks cavitation desinence and determines σ_d . Along with σ_i and σ_d , the values of σ at which travelling bubble cavitation changed into an attached cavity were also documented during this test.

Cavitation inception and desinence were called visually with the aid of a stroboscope to freeze the rapid motion of the bubbles for the eye. A number of factors rendered this method somewhat subjective, so alternative procedures were explored. All of these methods, including the difficulties associated with them, are discussed in Appendix B.

When considering vaporous cavitation, classical theory predicts that:

$$\sigma_i = \sigma_d = -C_{p_{\min}},$$

where $C_{p_{\min}}$ represents the minimum pressure on the model. This is

because it is only for $\sigma \leq -C_{p_{min}}$ that there exists any location on the model where $P \leq P_v$, with P being the pressure experienced by the cavitation bubble. This classical equation assumes that, for bubble growth: (1) the liquid pressure at the bubble wall does not depart from the equilibrium vapor pressure, and (2) the influence of surface roughness and viscous effects are negligible.

3.6 Air Content

Air content was measured in parts per million (ppm) of water on a molar basis with a Thomas Van-Slyke manometer apparatus. Fresh tap water has an air content of roughly 17 ppm, but operating the tunnel tended to lower this value until a stable level could be maintained somewhere below 12 ppm. Most engineering problems concerning cavitation encounter water having a relatively high air content. Consequently, the majority of tests in this investigation were conducted at an air content of approximately 10 ppm.

Furthermore, the pressure difference between cavitation inception and the development of an attached cavity decreases with lower air content. Hence, observations of cavitation noise dependence on pressure were facilitated by having a greater range of operation at the higher air contents. Noise measurements were attempted at a low air content of around 5 ppm for comparison, but the narrow range of pressure operation made trends extremely difficult to detect. The low air content was obtained by passing the water through a vacuum system which drove the air out of solution.

3.7 Investigation of Bubble Dynamics

A study of bubble dynamics was accomplished by taking high-speed motion pictures of travelling bubble cavitation on the Schiebe body. The photographic system was comprised of a Redlake Hycam camera with an EG & G Type 501 high-speed stroboscope. In conjunction with the motion pictures, the cavitation noise was recorded on a Bell and Howell Type CPR-4010 tape recorder.

The Hycam camera is a high-speed 16mm rotating prism camera that can attain framing rates of 11,000 pictures per second (pps). For the purposes of this experiment, it was found that a framing rate of around 1800 pps provided a sufficient number of pictures to document the growth and collapse cycle of each bubble observed. Also, a slower framing rate allows for a greater time interval to be recorded in each movie. At 1800 pps, a complete movie was filmed in just under one second.

Bubbles were more easily photographed when they appeared against a light background directly above and below the model as it is seen in profile. The best results were obtained by using backlighting to illuminate a white diffusing screen. This setup is shown in Figure 4.

The cavitation noise was detected using a small barium titanate transducer mounted in the surface of the model, as shown schematically in Figure 5. This model is pictured in Figure 2, where the transducer under discussion is the second one downstream. Urethane was chosen to mount the transducer because its acoustical properties approximate those of water. The signal from the transducer was amplified, high-pass filtered at 10 kilohertz (kHz), and recorded on magnetic tape.

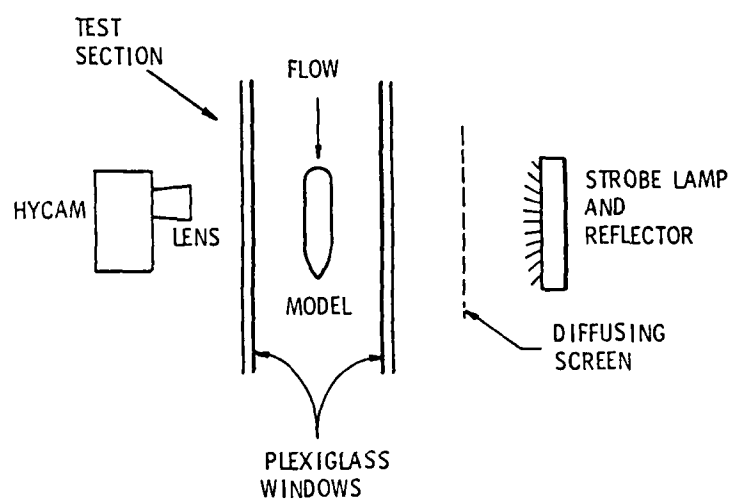


Figure 4. Schematic Arrangement of High-Speed Photographic Apparatus

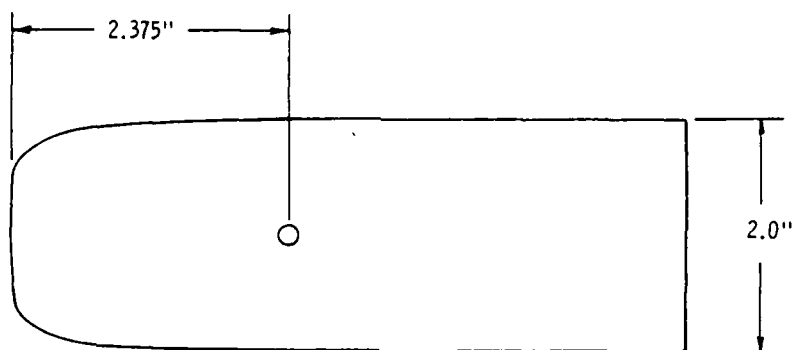


Figure 5. Illustration Depicting Location of
Acoustic Transducer Mounted in Schiebe Body

Recording was done at the maximum speed of 60 inches per second (ips) for later analysis at slower tape speeds.

It was important to be able to match the acoustic signal on tape exactly with each picture on the high-speed movies. This was done by employing the strobe used during the filming. When making a movie, the strobe would not commence firing until the camera approached the desired speed. It was then controlled by a rotating aperture inside the camera that fired the strobe once for every frame. Light from the strobe was collected by a photodiode and the signal was amplified and input to a second track on the tape recorder. Thus, each voltage spike on that track corresponded to a particular frame in the movie as well as to the acoustic signal on the other track. A schematic of this setup is shown in Figure 6.

Further studies of bubble dynamics were realized by filming the cavitation on video tape. A Sony Model AV-3400 camera and recording system were used for this purpose. At a constant velocity, the pressure in the test section was lowered from a point near cavitation inception down to where an attached cavity formed on the model. During each run, voltages pertaining to the test section pressure were continuously called out and recorded on the audio track of the video tape. In this manner, video tapes covering all stages of the travelling bubble cavitation process were obtained with the pressure documented throughout each film.

Both the high-speed motion picture studies and the video tape recordings were performed at velocities of 25, 30, and 35 fps. All three velocities were run with an air content of 10 ppm, while a run at 25 fps was also performed with an air content of 5 ppm.

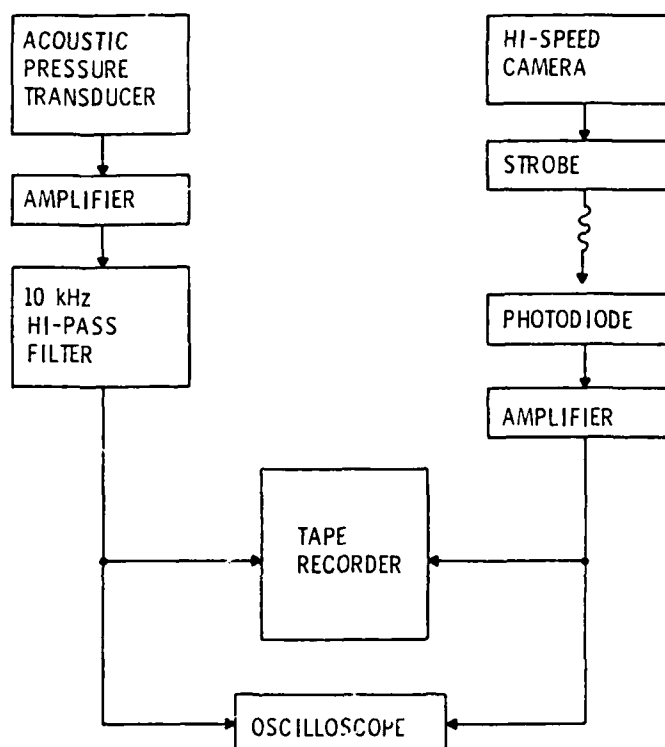


Figure 6. Schematic Diagram Depicting Setup for Recording Cavitation Noise to Accompany the High-Speed Movies

3.8 Noise Measurements

Noise measurements were conducted using a lead zirconate titanate hydrophone made at ARL/PSU. The hydrophone was mounted outside of the test section and acoustically coupled to the plexiglass window by means of vacuum grease. It was aimed at the center of the Schiebe body about two inches downstream from the nose as shown schematically in Figure 7.

The signal from the hydrophone was amplified and high-pass filtered at 10 kHz. After filtering, the signal was monitored with an oscilloscope, an integrating rms voltmeter, and a Spectral Dynamics SD-360 real time FFT processor. It was simultaneously recorded on the Bell and Howell tape recorder. A block diagram of this setup is shown in Figure 8.

The directivity of the receiving hydrophone was measured by using a Celesco LC-10 hydrophone as a calibrated sound source. Keeping a constant voltage white noise signal applied to the input of the LC-10, it was moved to a number of locations along the surface of the model. Voltages from the receiving hydrophone were recorded at each location on the rms voltmeter. Frequency spectra were also plotted for later calculation of the free field voltage response, but in this case, another LC-10 was used as the receiving hydrophone. This second LC-10 was used only for obtaining noise spectra. The LC-10 used for calibration in the test section was subsequently calibrated in an anechoic tank.

The LC-10 source was also used to emit tone bursts from a point near the model where cavitation would normally occur. In this way, some reverberant characteristics of the test section could be measured

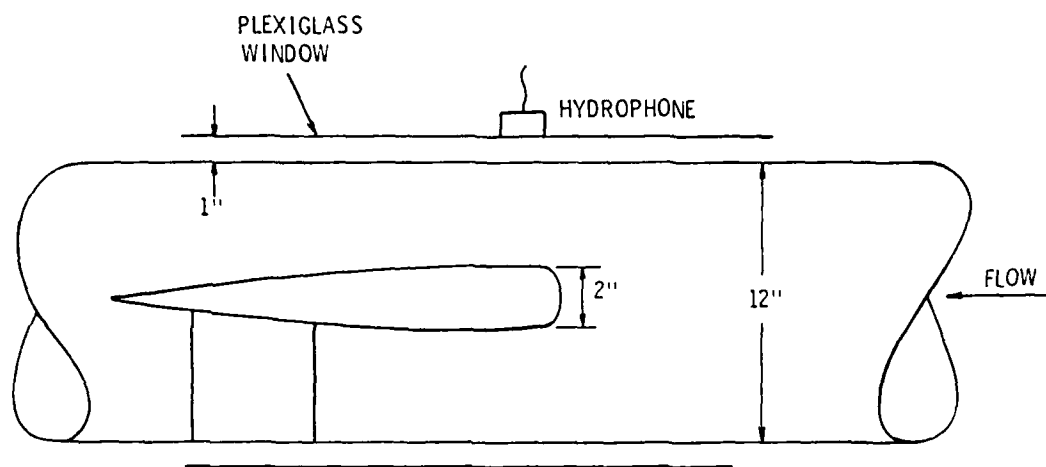


Figure 7. Illustration Depicting Location of Hydrophone Used for Measuring Cavitation Noise Level

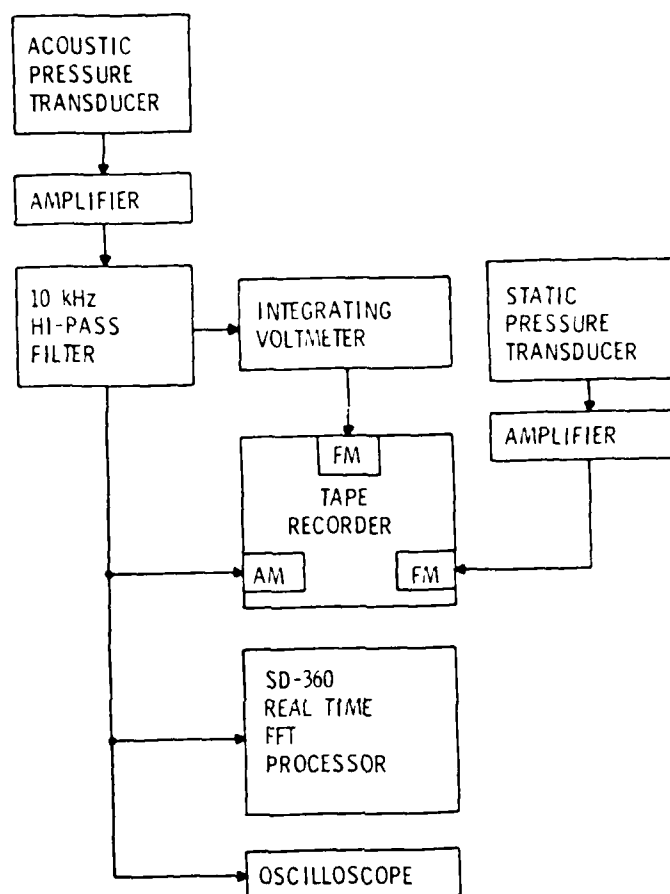


Figure 8. Schematic Diagram Depicting Setup for Recording Cavitation Noise Data

by photographing the response of the receiving hydrophone as seen on an oscilloscope. Finally, white noise was projected into the test section from the opposite side to that where the receiver was placed. By running the tunnel at 25 fps and lowering the pressure from a point well above inception, the test was intended to show how sound might be attenuated by bubbles that appear naturally in the free stream. The pressure was lowered until the cavitation noise itself became louder than the white noise which was being measured.

Not only was the total cavitation noise important, but also of interest was an indication of how much noise each individual bubble made as a function of pressure. Thus, a method had to be devised where the rate at which bubbles were collapsing and emitting noise bursts could be measured. Two techniques that failed to work are described in Appendix C. An attempt was even made to count the free stream bubble nuclei for correlation with the degree of cavitation activity. This is discussed in Appendix D. It was finally decided to tape record the entire test for later analysis.

The Bell and Howell tape recorder could operate in a frequency modulation mode that was ideal for accurately recording DC voltages on any selected channels. While the cavitation noise was being recorded on one channel, a DC output proportional to the reading on the rms voltmeter was input to a second channel. On yet a third channel was recorded an attenuated output from the transducer which monitored the static pressure in the test section. The reader is again referred to Figure 8. Thus, by counting the number of bursts on the noise channel whose rms noise level was recorded on the second channel, both the

number of events occurring and their average noise level were known as functions of pressure.

With the velocity held constant, the pressure in the test section was lowered slowly from an initial value above p_1 . As soon as noise bursts due to bubble collapse were first witnessed on the oscilloscope, tape recording commenced at 60 ips. The pressure was continuously lowered until an attached cavity formed on the model, at which point the recorder was turned off. Seven different velocities were tested in this manner from 25 to 40 fps in increments of 2.5 fps.

CHAPTER IV

RESULTS

4.1 Pressure Distribution on the Schiebe Body

As discussed in Section 3.2, the shape of a Schiebe body is determined from the profile of streamlines created by the addition of a disk source to a uniform flow. A closed form solution of this profile has not been found, so a computer is used to generate the coordinates defining the surface of the model. This data is then used to generate values of the pressure coefficient C_p as a function of position along that surface.

The ten values of C_p that were determined experimentally are shown, along with the theoretical curve generated by computer, in Figure 9. Each point has associated with it a negligible standard deviation after six runs at five different velocities, and the agreement with the predicted values is seen to be quite good. The abscissa in Figure 9 is a dimensionless length, s/a , found by normalizing the distance from the stagnation point defined by the arc length along the surface, by the maximum radius of the model. Since the maximum radius is one inch, the abscissa is correctly scaled for measurement of inches along that surface.

A least squares polynomial curve fitting routine was employed to describe the theoretical C_p versus s/a curve. The curve was broken into three segments which were joined by cubic equations to insure continuity of the function and its first derivative. Results from this

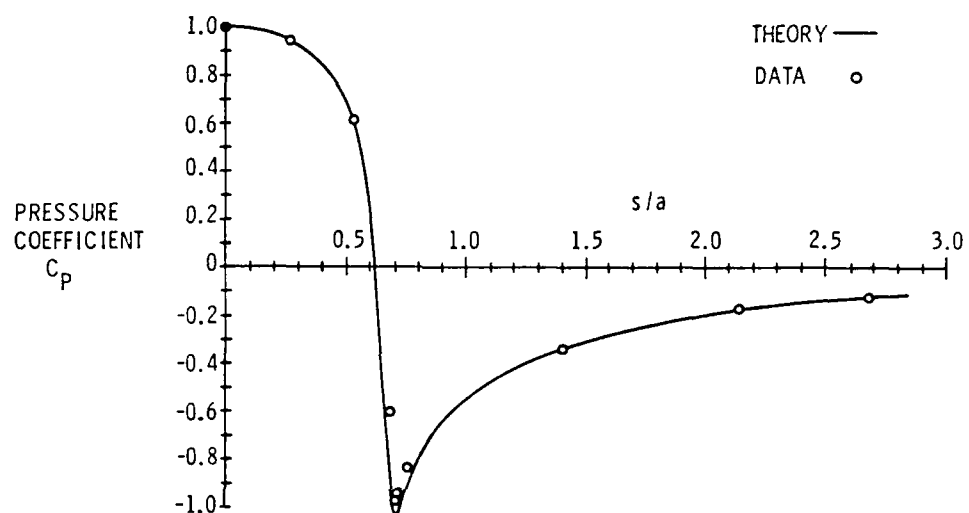


Figure 9. Theoretical and Experimental Values of C_p vs. s/a

procedure are listed in Table 1. These equations are necessary for computer solutions of the Rayleigh-Plesset equation.

4.2 Cavitation Inception and Desinence

Results obtained for cavitation inception and desinence are presented in Figure 10. Problems involved with calling cavitation visually are manifested in the large standard deviation. The margin of error was largest at lower velocities where the free stream pressure P_∞ must be very low to cause cavitation. At these pressures, free stream air bubbles become large enough to be confused with cavitation on the model. Difficulties of this nature encountered at low pressures might explain the dip in the curves at 27.5 fps.

The point at which travelling bubble cavitation transforms into an attached cavity is denoted by Attached Cavity σ_i . Note that this parameter remains relatively constant with velocity. It can be seen how the operating pressure range that can support travelling bubble cavitation diminishes as the velocity is increased. Also, the cavitation hysteresis phenomenon is illustrated by the desinent pressure being higher than the incipient pressure.

Probably the most interesting feature of Figure 10 comes from a comparison with Figure 9. Recalling Section 3.5, it seems that vaporous cavitation should exist only for $\sigma \leq -C_{p_{min}}$, where $C_{p_{min}}$ is the minimum point on the C_p curve. In other words, $\sigma > -C_{p_{min}}$ states that there is no location along the surface of the model where $P \leq P_v$, a condition which is theoretically required for vaporous cavitation. The Schiebe body used in this study has $C_{p_{min}} = -1.03$.

TABLE 1
EQUATIONS DEFINING C_p ALONG
SURFACE OF SCHIEBE BODY

$$i) \quad 0 \leq \frac{s}{a} \leq 0.625$$

$$\begin{aligned} C_p = & -69.621 \left(\frac{s}{a}\right)^7 - 79.022 \left(\frac{s}{a}\right)^6 + 177.71 \left(\frac{s}{a}\right)^5 \\ & - 90.038 \left(\frac{s}{a}\right)^4 + 13.037 \left(\frac{s}{a}\right)^3 + 0.085253 \left(\frac{s}{a}\right)^2 \\ & - 0.25309 \left(\frac{s}{a}\right) + 1.0068 \end{aligned}$$

$$ii) \quad 0.625 \leq \frac{s}{a} \leq 0.650$$

$$C_p = 165.00 \left(\frac{s}{a}\right)^3 - 438.02 \left(\frac{s}{a}\right)^2 + 342.68 \left(\frac{s}{a}\right) - 83.389$$

$$iii) \quad 0.650 \leq \frac{s}{a} \leq 0.745$$

$$C_p = 122.46 \left(\frac{s}{a}\right)^2 - 176.80 \left(\frac{s}{a}\right) + 62.786$$

$$iv) \quad 0.745 \leq \frac{s}{a} \leq 0.770$$

$$C_p = 717.29 \left(\frac{s}{a}\right)^3 - 1697.7 \left(\frac{s}{a}\right)^2 + 1340.9 \left(\frac{s}{a}\right) - 354.26$$

$$v) \quad \frac{s}{a} \geq 0.770$$

$$C_p = \frac{0.330}{0.390 - \left(\frac{s}{a}\right)}$$

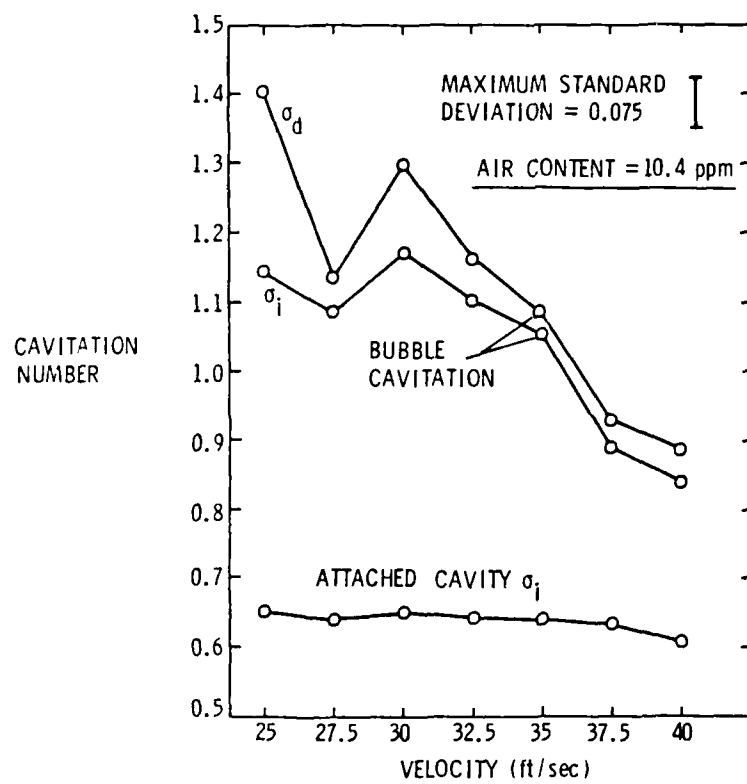


Figure 10. Values of σ_i and σ_d for Travelling Bubble Cavitation, and Values of σ_i for an Attached Cavity, As Functions of V_∞

A possible explanation is that cavitation nuclei containing gas having internal pressure such that $P_G > P_v$ pass through a region with local pressure $P < P_G$ that may cause the nuclei to grow enough to be confused with vaporous cavitation. For instance, $\sigma = 1.1$ at a velocity of 25 fps indicates a minimum pressure of about 0.05 atm on the surface of the model. This in turn would imply $P_G \approx 0.05$ atm as compared with $P_v \approx 0.03$ atm. However, as the bubble grows, P_G varies either as $1/R^3$ for isothermal expansion, or as $1/R^4$ if the expansion is adiabatic. This is a consequence of the gas diffusion through the bubble wall being insignificant in relation to the rate of bubble growth and collapse. P_v remains essentially constant during bubble growth in cold water, and thus vaporous cavitation will dominate as the pressure is lowered. The temperature of the water used throughout this investigation was approximately 70°F.

4.3 Analysis of Bubble Dynamics

Data acquired by tape recorder while taking high-speed films of bubble collapse were analyzed by digitization on a DEC System-10 computer using an EAI 693 analog interface. By playing the tape back at 15/16 ips after having recorded at 60 ips and then sampling at 1.5 kHz, an effective sampling rate of 96 kHz was achieved. Both the channel with the acoustic signal and the channel having the timing pulses were analyzed simultaneously so that temporal coordinates for the acoustic signal were not lost. Every tenth timing pulse was widened by a monostable multivibrator to facilitate counting.

The run that best illustrates bubble growth and collapse was that performed at 25 fps with an air content of 4.6 ppm. At such a low air

content in addition to the low velocity, a very low pressure is required for cavitation. Low air content allows for less and smaller cavitation nuclei becoming available for cavitation bubble growth in the low pressure zone. Once growth commences, the lower pressure supports larger maximum bubble radii than would occur at higher air contents.

Figure 11 shows photographs of a bubble in water having an air content of 4.6 ppm, with $V_{\infty} = 25$ fps and $\sigma = 0.62$. A plot of the bubble volume as a function of s/a appears in Figure 12. The bubble volume was calculated by measuring the length and width of the bubble as seen along the profile of the model. Next, the volumetric shape was assumed to be an ellipsoid which is symmetrical about an axis perpendicular to the surface of the model. Finally, an effective radius may be determined by calculating the radius of a sphere having a volume equivalent to that of the bubble.

Note that the bubble becomes visual around $s/a = 1.0$, just as it leaves the region where $P < P_v$. This region is determined from Figure 9 where $C_p < -\sigma$. It appears that most of the growth stage results from inertial effects after an initial acceleration produced by $P < P_v$. This type of behavior is predicted by solutions of the Rayleigh-Plesset equation.

Frames 10 through 13 of Figure 11 depict the rebound of the bubble into another growth and collapse cycle. Other investigators have observed numerous rebounds resulting from a single bubble. As was previously discussed, it seems that rebounding results from noncondensable gases contained within the bubble. In this study, rebounding was found to be common only at the low air content, with

Frame

1

2

3

Figure 11. High-Speed Photographs of Cavitation Bubble with
 $V_{\infty} = 25$ fps , $\phi = 0.62$, and Air Content of 4.6 ppm

Frame

4

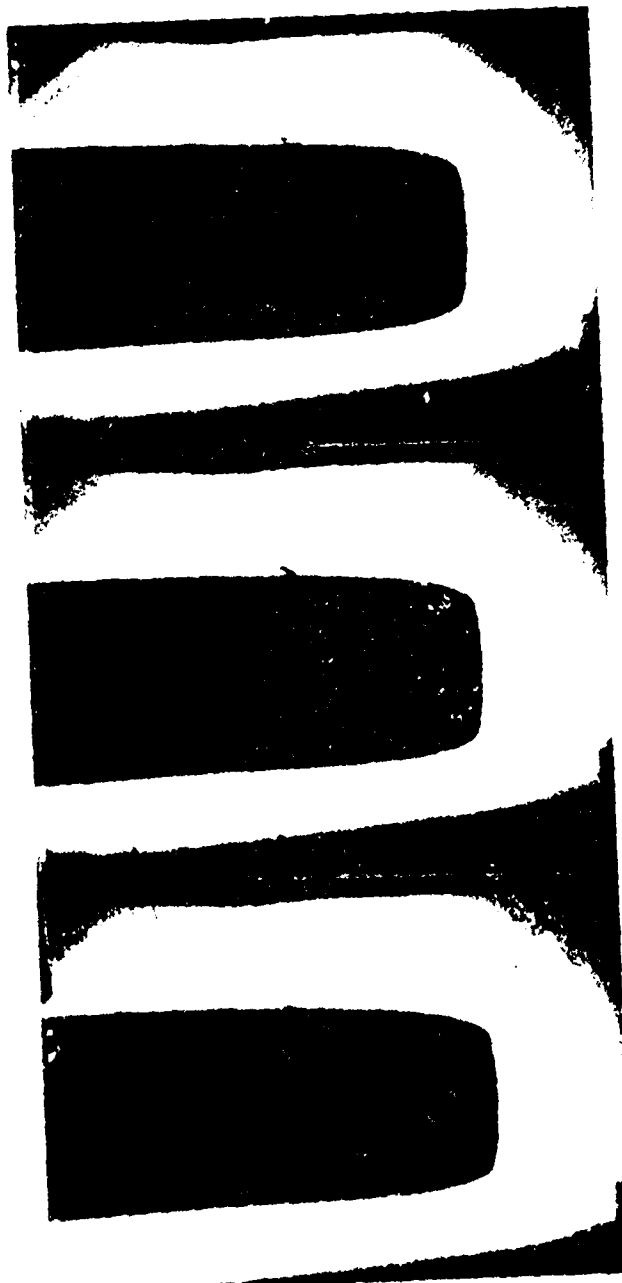
5

6

Figure 11. (continued)

Frame

Figure 11. (continued)

Frame

10

11

12

Figure 11. (continued)

Frame

Figure 11. (continued)

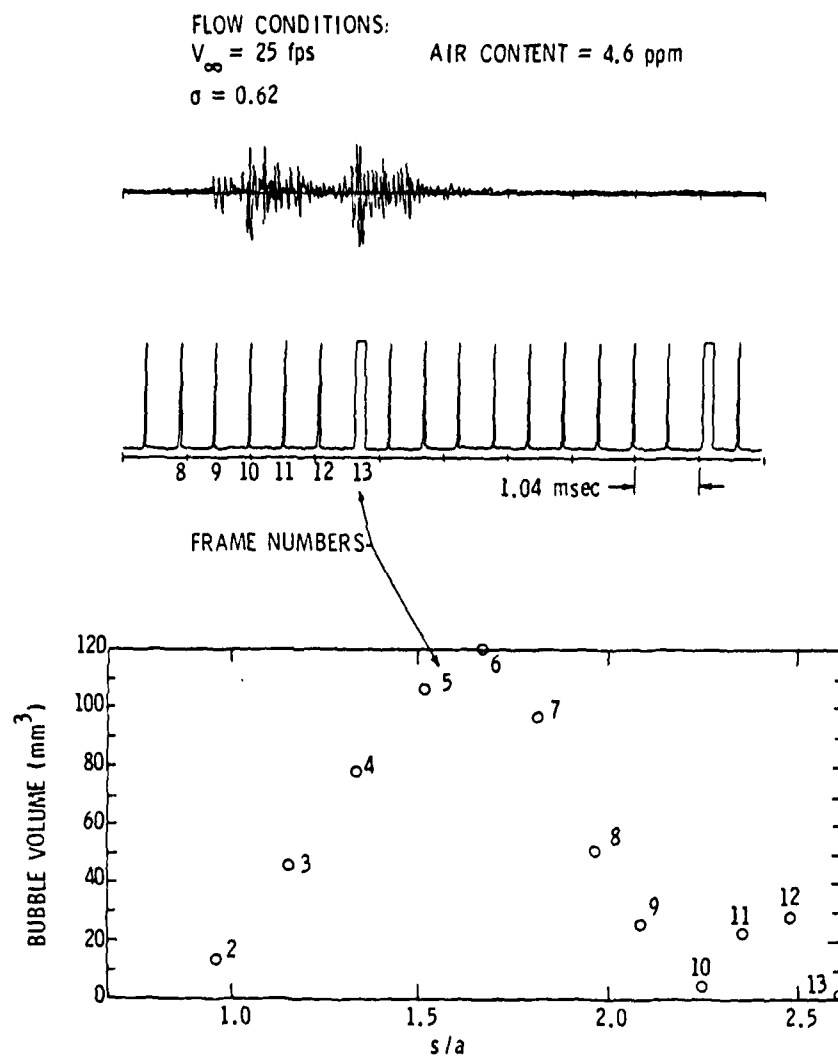


Figure 12. Acoustic Signal and Bubble Volume Plot That Accompany Photographs in Figure 11

some small rebounds occurring for high air content at 25 fps, but none at the higher velocities.

Included in Figure 12 is a trace of the sound recorded from the bubble shown in Figure 11. The location of the receiving transducer on the surface of the model was close enough to the bubble that the time required for the sound to arrive at the transducer may be neglected. It can be seen that sound is just beginning to be received around Frame 9 where the bubble has almost completed its collapse stage. This might be due to the bubble on the underside of the model. The major contribution to the sound pulse arrives in the next frame where collapse has ended and growth from the rebound has begun. A second pulse is emitted as the rebound collapses in Frame 13.

Figure 12 confirms the fact that the majority of sound is emitted during the final moments of collapse. No sound emission was observed during any growth stage. Very often, a small amount of sound will precede the larger pulse that constitutes the dominant acoustic output. One possible explanation is that bubbles do not always collapse in a roughly spherical fashion, and an abrupt indentation on one side of a bubble might itself generate sound. The finer details of the pulse are obscured by transducer resonance. It was not practical to filter this resonance since it occurred in the neighborhood of 20 kHz, which is a region where cavitation noise is very significant.

The most interesting observation to be made concerning the emitted sound is that the acoustic energy resulting from the collapse of the rebound is roughly equivalent to that of the initial collapse. This seems to contradict the theories which predict the energy to vary with some positive power of R_M . Recalling Figure 9, collapse of the

rebound occurs in a pressure region given by $C_p = -0.11$ that is higher than the pressure region of the initial collapse having $C_p = -0.15$. This will cause the rebound to experience a more violent collapse. Also, the collapse of the rebound occurs somewhat closer to the transducer than the initial collapse. This combination of factors might compensate for an effective R_M of the initial growth cycle being 1.6 times that of the rebound. In any event, the implication is that the rebound phenomenon should be incorporated into cavitation noise theories which use parameters such as cavitation nuclei concentration to indicate the number of bubbles that are emitting sound.

Shown in Figure 13 are the photographs of a bubble in a 25 fps flow with an air content of 10.0 ppm and $\sigma = 0.68$. Note the number of free stream bubbles that are not part of the cavitation process. From Figure 10 it is seen that the pressure at which the photographs were taken is as low as possible while still supporting travelling bubble cavitation. These photographs thus represent the maximum concentration of cavitation bubbles on the model encountered at any one time during this investigation. Nevertheless, it is apparent that the cavitation bubbles are sufficiently far apart to justify analysis of them as independent events.

Figure 14 shows the acoustic signal and bubble volume plot that accompany the photographs in Figure 13. Again, a sound pulse is associated with the final moment of collapse. The rest of the sound pulses in the figure are due to other bubbles on the model. In comparison with Figure 12, the bubble volume plot of Figure 14 is typical in that it shows a smaller effective R_M and shorter bubble lifetime than would be expected at a lower air content under similar

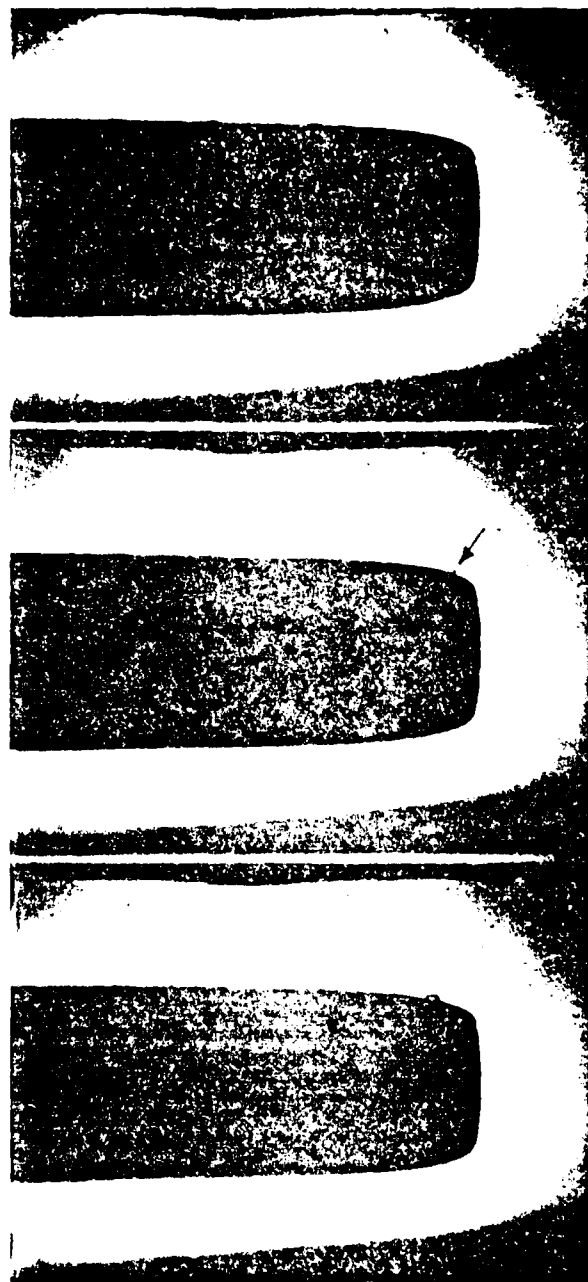
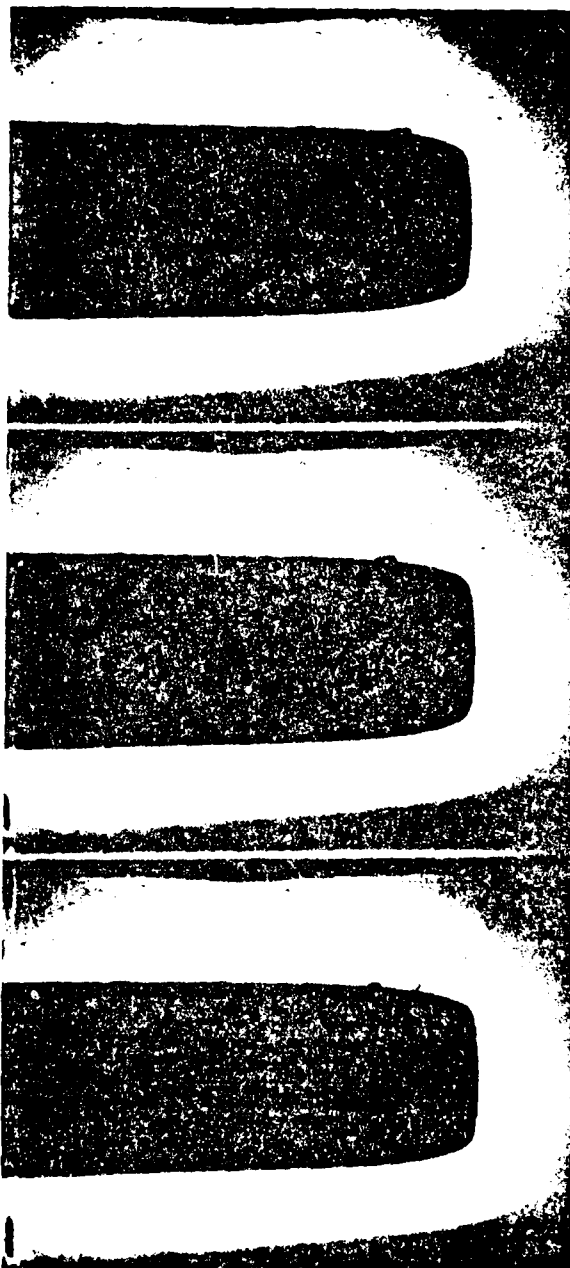


Figure 13. High-Speed Photographs of Cavitation Bubble with $V_{\infty} = 25$ fps, $\beta = 0.68$, and Air Content of 10.0 ppm

Frame

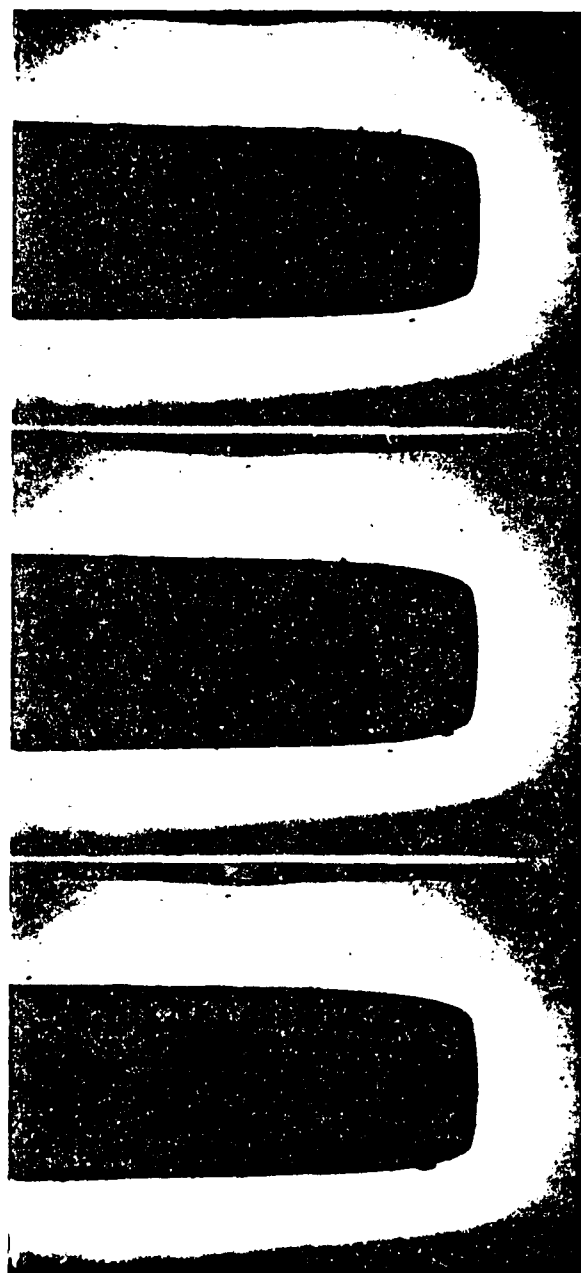


4

5

6

Figure 13. (continued)

Frame

7

8

9

Figure 13. (continued)

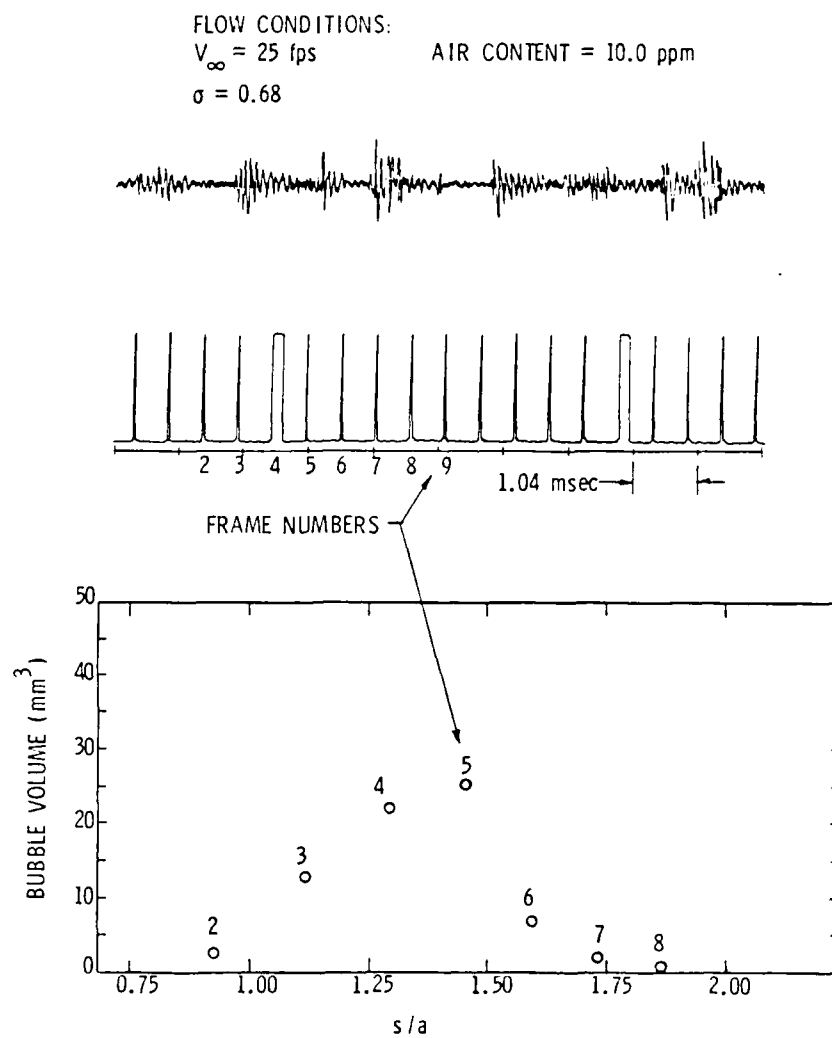


Figure 14. Acoustic Signal and Bubble Volume Plot
That Accompany Photographs in Figure 13

conditions. In all cases, the films were taken at pressures just above those which would cause the cavitation to be attached to the body.

Similar films were also taken at 30 and 35 fps with an air content of 10.0 ppm. These films did not produce any new information. The trend was for the typical effective R_M and bubble lifetime to decrease somewhat as the velocity was increased. At higher velocities, it became increasingly difficult to resolve the acoustic pulses from one another, where transducer resonances were often observed to last as long as 5 msec. It is believed that the increased flow velocities were responsible for these prolonged resonances, but the exact nature of the cause is unknown.

To attain a more statistical approach to the matter of bubble dynamics, average growth curves were obtained from the video tapes of cavitation. One problem with this method is that the poor resolution of the television screen places a lower bound on the size of bubbles that can be measured. Similarly, difficulties arise in marking the exact position where the edges of the bubbles are located.

Bubbles on video tape were most easily measured against the surface of the model, as opposed to along the profile as was done when analyzing the high speed films. When looking in a direction that is normal to the model surface, the bubbles appear to be circular. When seen in profile, they appear to be elliptical. This results from the bubble flattening out along a surface of similar streamlines as it becomes larger. Thus, smaller bubbles tend to be more spherical than the larger ones, and in general, the flattening is more pronounced at

the higher velocities. Since only the circular projection could be seen on the video tapes, a bubble volume was difficult to obtain without knowledge of the third dimension.

The surface of the model was broken up into a number of regions where bubble diameters were measured and averaged. Figures 15 through 18 show the results of tests run at 25 fps with a 4.6 ppm air content, and at 25, 30 and 35 fps with a 10.0 ppm air content. The range of cavitation numbers presented in these figures corresponds to those locations on the video tape where data interpretation was most conveniently performed. Error bars attached to the points indicate the standard deviation, which reflects the scatter about the mean bubble diameter calculated for that particular region.

The salient features of Figures 15 and 16 resemble those of the specific examples depicted in Figures 12 and 14 for $V_{\infty} = 25$ fps. Figure 15 clearly shows frequent rebounding action for the low air content, while Figure 16 merely hints at it for the high air content. Although the maximum diameters are approximately the same for all three velocities at high air content, the large differences in σ prohibit any direct comparisons.

Most importantly, the graphs show where cavitation occurs on the model, and also allow for crude estimates to be made of the growth and collapse times. It was not practical to cover any significant range of σ for each velocity. This was because, at lower pressures, the video tape superimposed the bubbles upon each other due to afterimaging of the greater cavitation activity. At higher pressures, the bubbles were too small to produce a meaningful curve from a television screen.

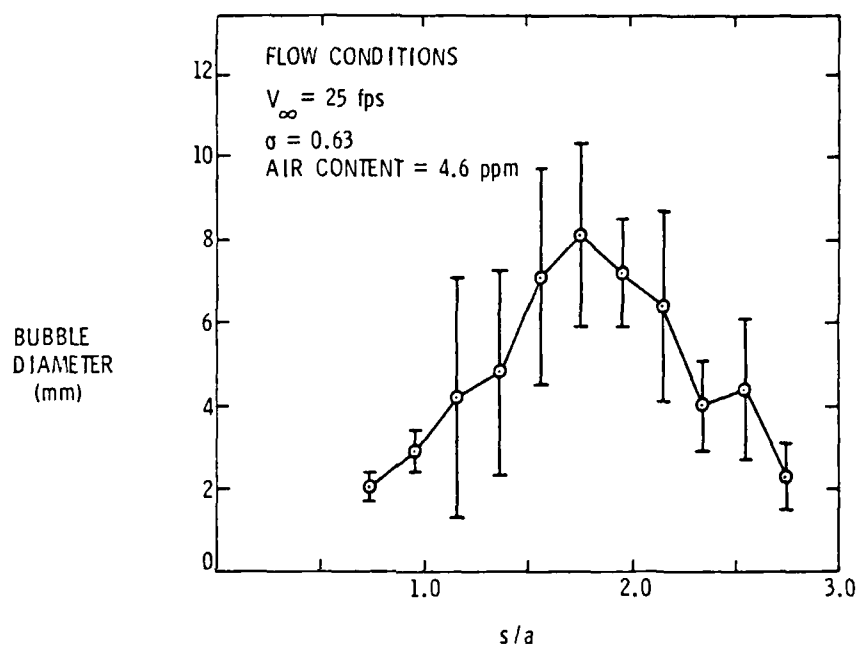


Figure 15. Bubble Diameter Plot at $V_{\infty} = 25$ fps, $\sigma = 0.63$, and Air Content at 4.6 ppm

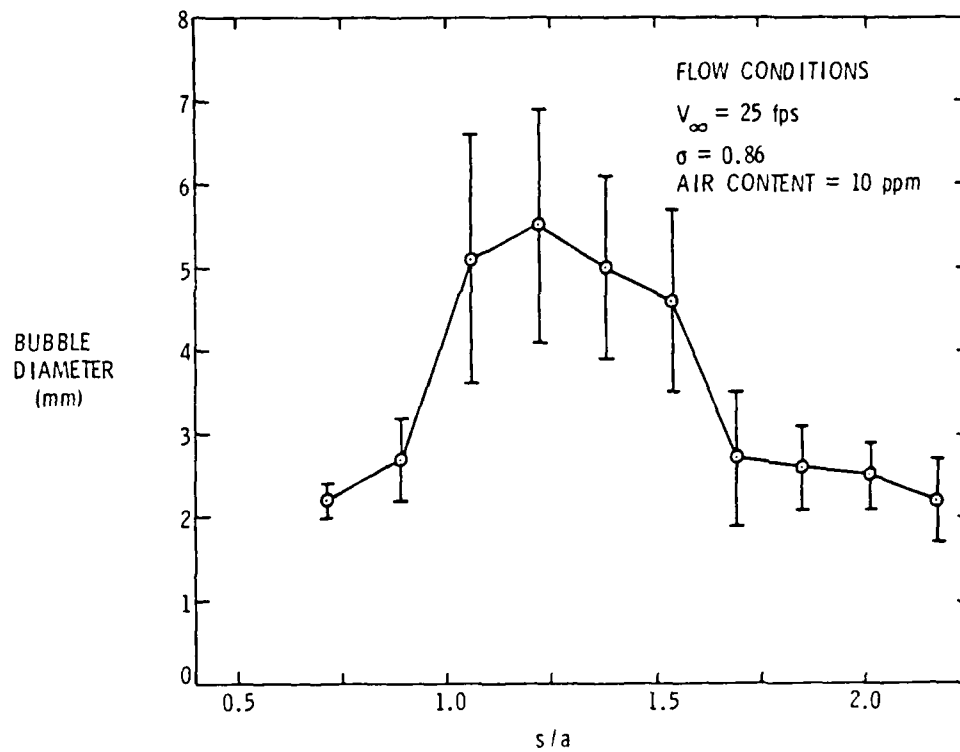


Figure 16. Bubble Diameter Plot at $V_{\infty} = 25$ fps ,
 $\sigma = 0.86$, and Air Content of 10 ppm

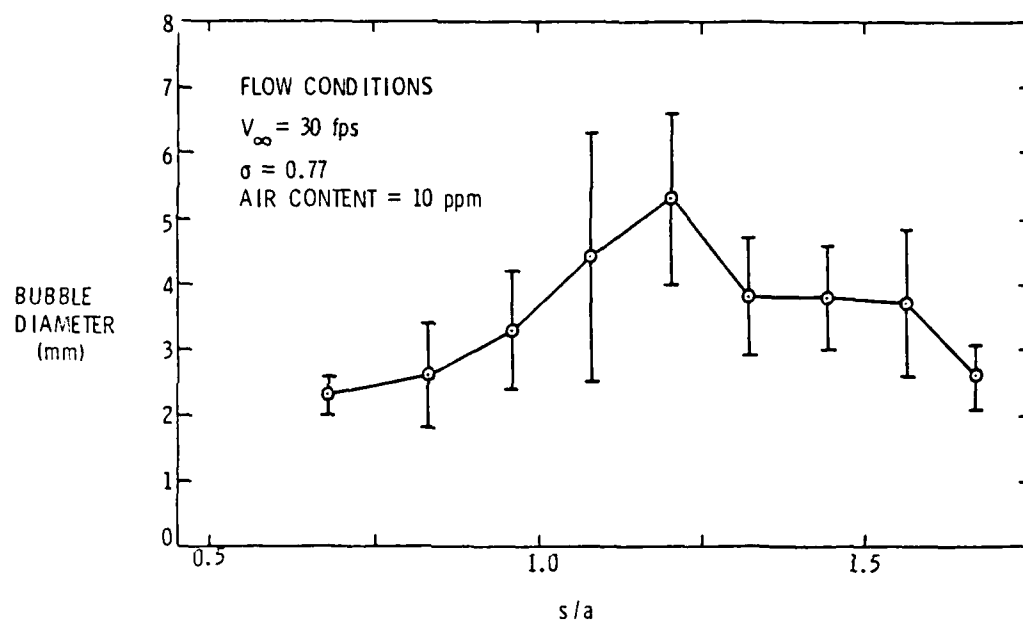


Figure 17. Bubble Diameter Plot at $V_{\infty} = 30 \text{ fps}$,
 $\sigma = 0.77$, and Air Content of 10 ppm

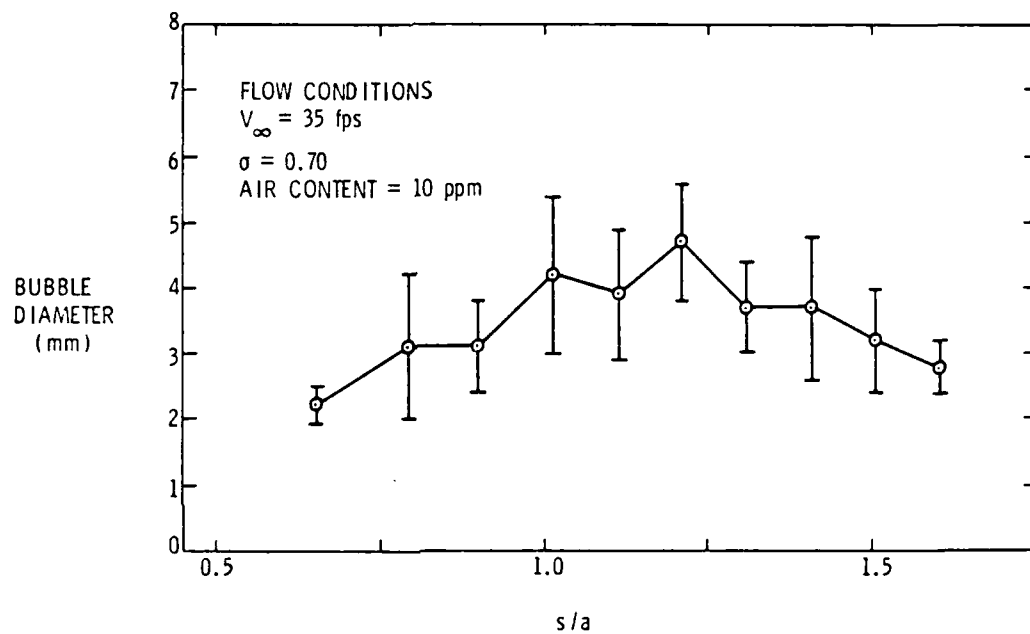


Figure 18. Bubble Diameter Plot at $V_{\infty} = 35$ fps ,
 $\sigma = 0.70$, and Air Content of 10 ppm

4.4 Cavitation Noise

After examination of the results in the previous section, it was decided that the transducer mounted in the model was inadequate for making noise measurements. Besides the problem of prolonged ringing, the transducer seemed to be located too close to where collapse was occurring. Consequently, noise measurements were obtained with a hydrophone having a one-inch diameter active element that was acoustically coupled to the outside of the test section window.

The directivity of the hydrophone to an omnidirectional white noise source as a function of axial distance along the model is shown in Figure 19. At the 3 dB down points, the beamwidth is about 3 inches on the model at the location of maximum cavitation activity. Recall that the noise was being high pass filtered at 10 kHz.

In Figure 20 are presented the photographs taken of the response of the water tunnel and hydrophone to an acoustic impulse generated near where cavitation occurs on the model. The upper trace in Figure 20a shows one cycle of a 25 kHz sinusoid being input to the source. In the lower trace of that same photograph, the initial response of the receiving hydrophone is seen to occur after a delay of 0.12 msec. This corresponds to a distance of 7.0 inches travelled by sound in water. With a test section radius of 6.0 inches and a plexiglass test section window thickness of 1.0 inch, the delay corresponds to the direct transmission of sound.

The next impulse is received 0.34 msec after being emitted by the source. This represents a distance of 20 inches travelled by the sound, or 13 inches in excess of the direct path. In this case, reflection most likely occurred off of the air-plexiglass interface

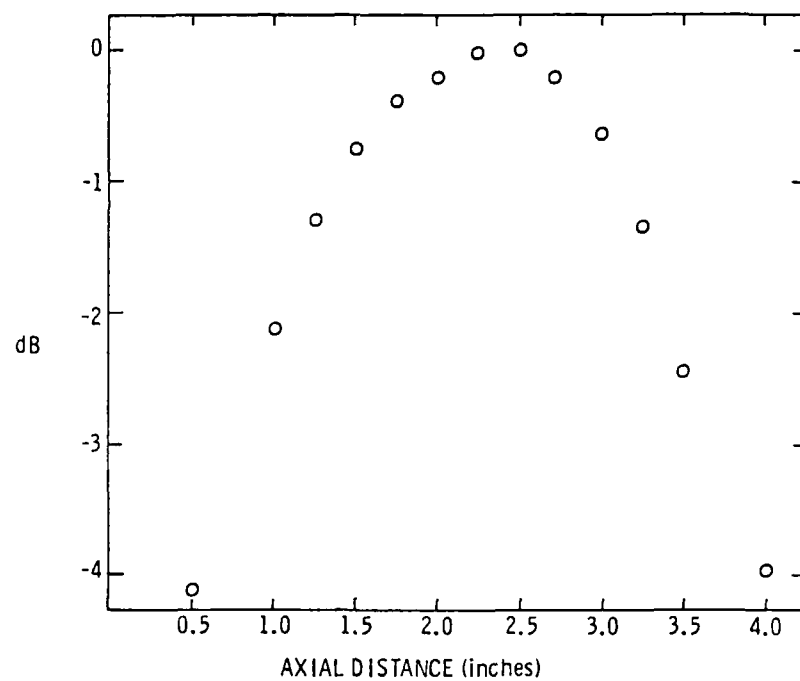
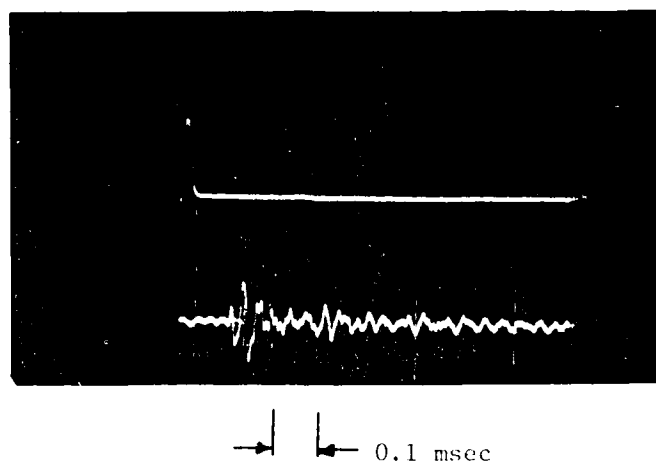
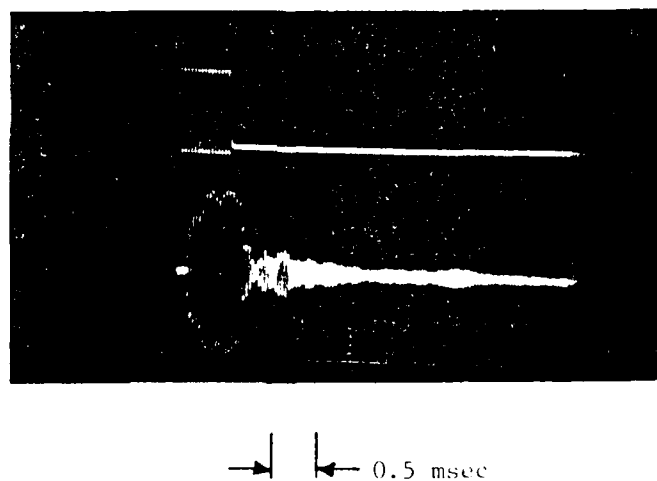


Figure 19. Hydrophone Beamwidth at Location of Model



(a)



(b)

Figure 20. Response of Hydrophone to (a) 1 Cycle of a 25 kHz Sinusoid, and (b) 16 Cycles of a 25 kHz Sinusoid; Both Generated Adjacent to Model in Test Section

created by the window on the opposite side of the tunnel from the hydrophone. A reflection such as this would indeed define a transmission path which is three times as long as the direct path. The direct and primary reflection paths are illustrated in Figure 21. Other reflections in Figure 20a were lost in the unavoidable transducer ring, but were probably so low as to be insignificant.

Figure 20b shows the response of the hydrophone to 16 cycles of a 25 kHz sinusoid. After a steady state was reached, the source was turned off and presumably the reverberant sound field in the test section would decay exponentially. Of course, both the source and the receiver will exhibit their own transient responses. It is interesting to see how the decay envelope of the response appears to be modulated. In fact, the decay envelope seems to first go to zero before it rises again to a new secondary peak about 0.4 msec later. After that, the decay seems more normal with only minor oscillations in the envelope. This initial null in the decay becomes important when cavitation noise pulses are counted.

To determine if sound might be attenuated by free stream bubbles during its passage through the test section, white noise was projected into the tunnel through a window on the side opposing the receiving hydrophone. The test section flow velocity was chosen to be 25 fps because lower pressures are required for cavitation as the velocity is decreased. In addition, the air content was maintained at 10 ppm. Hence, these lower pressures at high air content allow for larger bubbles to exist in the free stream where sound absorption will occur; see, for example, Figure 13. The pressure was lowered at this velocity until cavitation noise itself obscured the injected white noise.

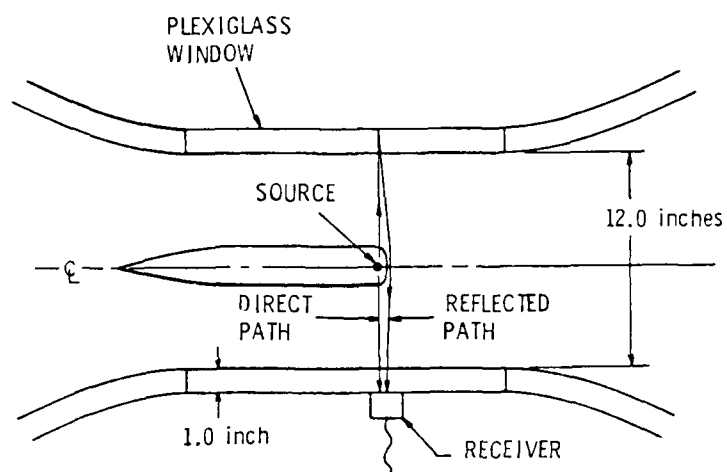


Figure 21. Illustration Depicting Direct and Primary Reflection Paths Followed by Sound Generated Adjacent to Model in Test Section

Figure 22 shows that the attenuation as a function of pressure is negligible in amounting to less than one decibel over the entire range of observation. Again, the receiver was high pass filtered at 10 kHz.

As discussed in Section 3.8, a tape recording was made of cavitation noise along with information about the rms noise level and the static pressure in the test section. Digitization was again performed, but this time with a more efficient routine which provided an effective sampling rate of 200 kHz. At this rate, the sampling routine could digitize continuous segments of the acoustic signal for 185 msec in real time, while also sampling the noise level and pressure immediately before and after each sampled acoustic signal. The cavitation noise pulses were then displayed on a screen where they could be counted and plotted.

Reproductions of some typical cavitation noise pulses encountered at a velocity of 30 fps are presented in Figures 23 through 25. In Figure 23, only one bubble would be counted. The reasoning for this assumes that the first little pulse was emitted during the same collapse that produced the large pulse that followed. Also, the third pulse seems to be the result of the null in the decay envelope as was discussed in reference to Figure 20b.

On the other hand, three pulses would be counted in Figure 24 since the third pulse is considered of sufficient size as not to be part of the decay of the second. Obviously, there were many more cases where it was by no means clear whether or not a number of neighboring pulses originated from the same bubble. Hence, there was a significant degree of subjectivity involved in the counting procedure.

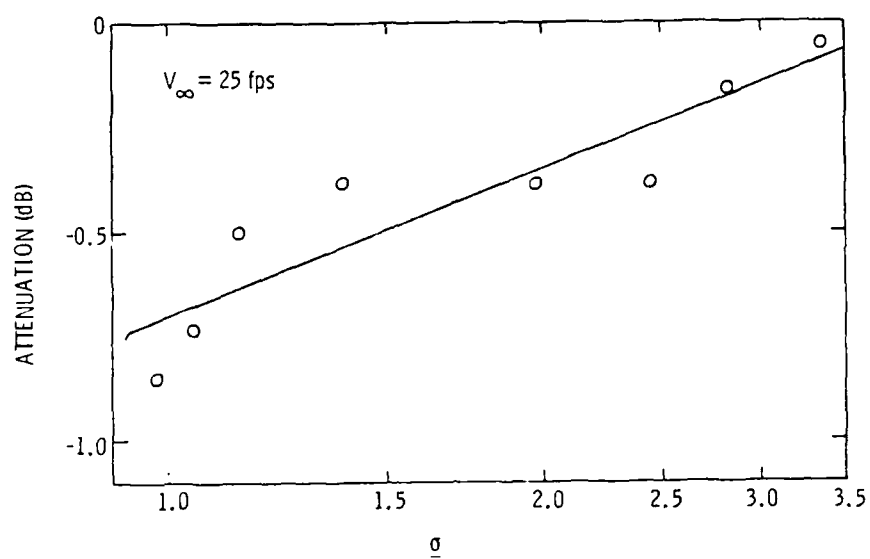


Figure 22. Attenuation of Sound by Free Stream Bubbles

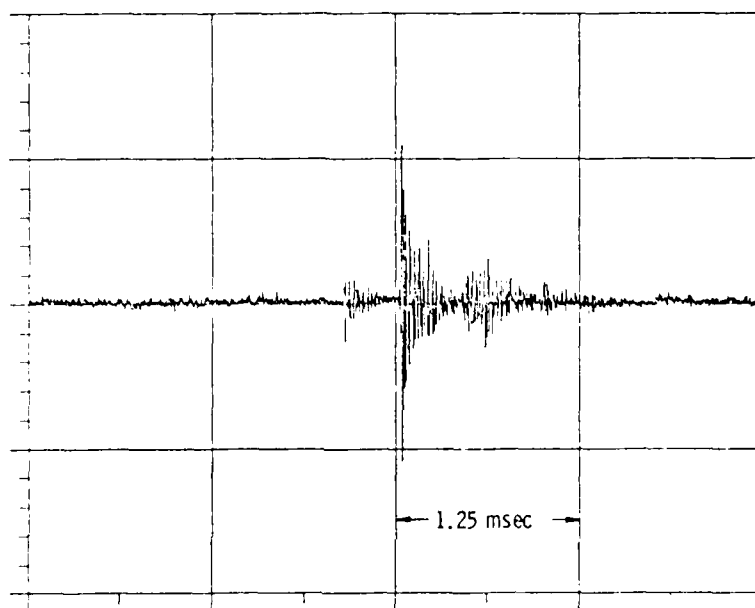


Figure 23. Example of Cavitation Noise Signal

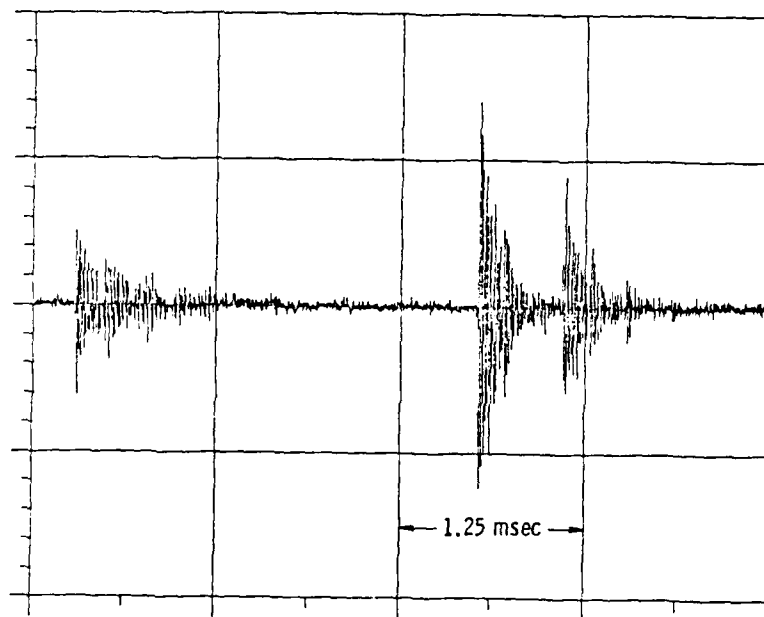


Figure 24. Example of Cavitation Noise Signal

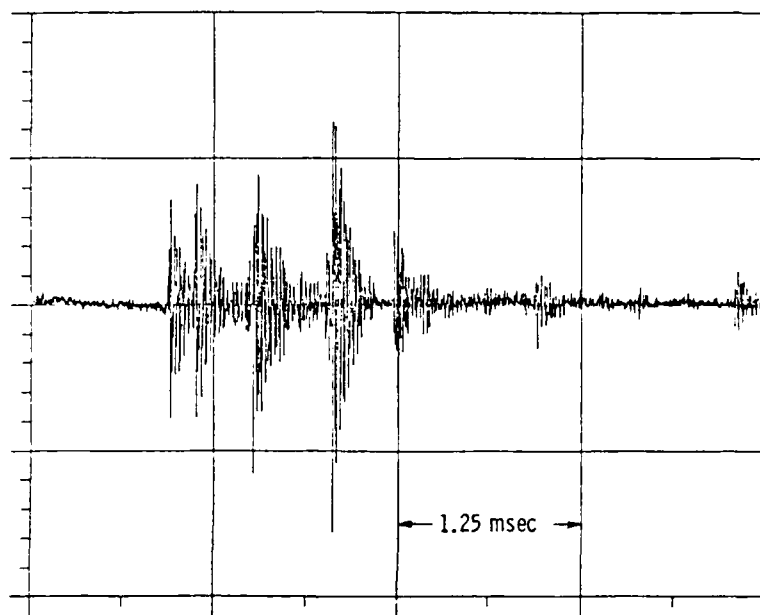


Figure 25. Example of Cavitation Noise Signal

Figure 25 shows a situation where a number of noise pulses are found clustered together. Analysis of the high-speed film indicated that the bubbles should collapse independently of each other. However, the occasional occurrence of these clusters suggests something more than random events. One explanation might be that large bubbles split into smaller ones which emit their own noise pulses. Also, the possibility of rebounds cannot be ruled out. Whatever the reason, the bursts should be counted as separate events for the purpose of ultimately determining how much noise is emitted by each bubble.

To better understand how the noise pulses are distributed, an entire 185 msec record was analyzed for the time between successive noise bursts. About 130 bursts in all were counted in this example at 30 fps, with the results plotted in Figure 26. The histogram is seen to have roughly the form of a Poisson distribution, which, as discussed in Section 2.1, is a sufficient condition for using single bubble collapse theories to describe the cavitation noise.

Figures 27 through 30 along with Table 2 display results yielded by the digitization procedure. Curves obtained for the number of cavitation noise events per second N as a function of σ are presented in Figure 27. Plots at 25 and 27.5 fps do not appear because of extreme difficulties encountered in trying to distinguish different pulses. Along the abscissa, σ was normalized by σ_d , which is different for each velocity. Plotting both σ/σ_d and N in terms of their logarithms produced relatively straight lines which suggest simple exponential relations. Lines drawn through the data to fit the majority of points in a mean square sense show these slopes to be quite similar to each other. The functional relationships between N and σ as deduced from the slopes appear in Table 2, the average of which is $N \sim \sigma^{-10.6}$.

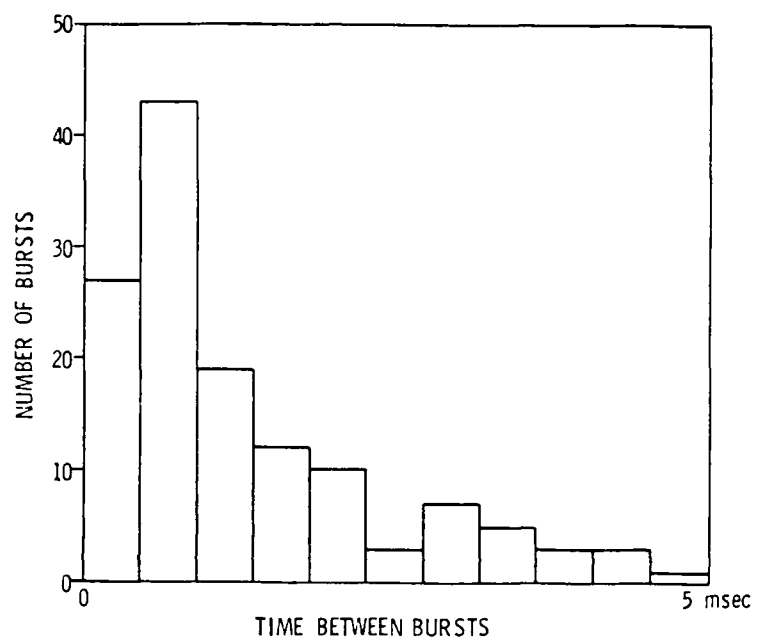


Figure 26. Noise Burst Interval Distribution

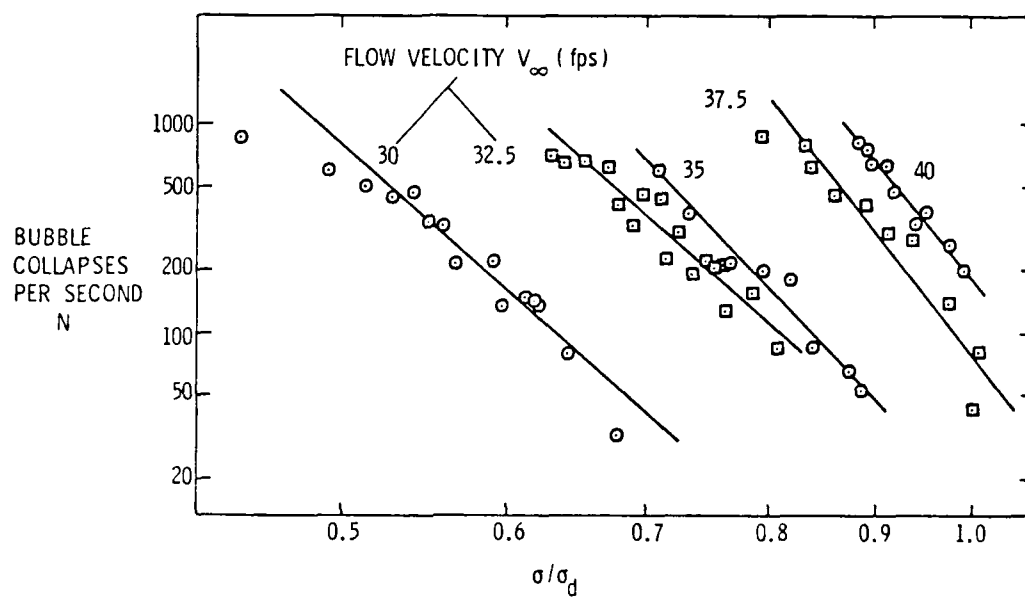


Figure 27. Number of Noise Bursts Per Second Versus σ/σ_d at Velocities from $V_\infty = 30$ to 40 fps

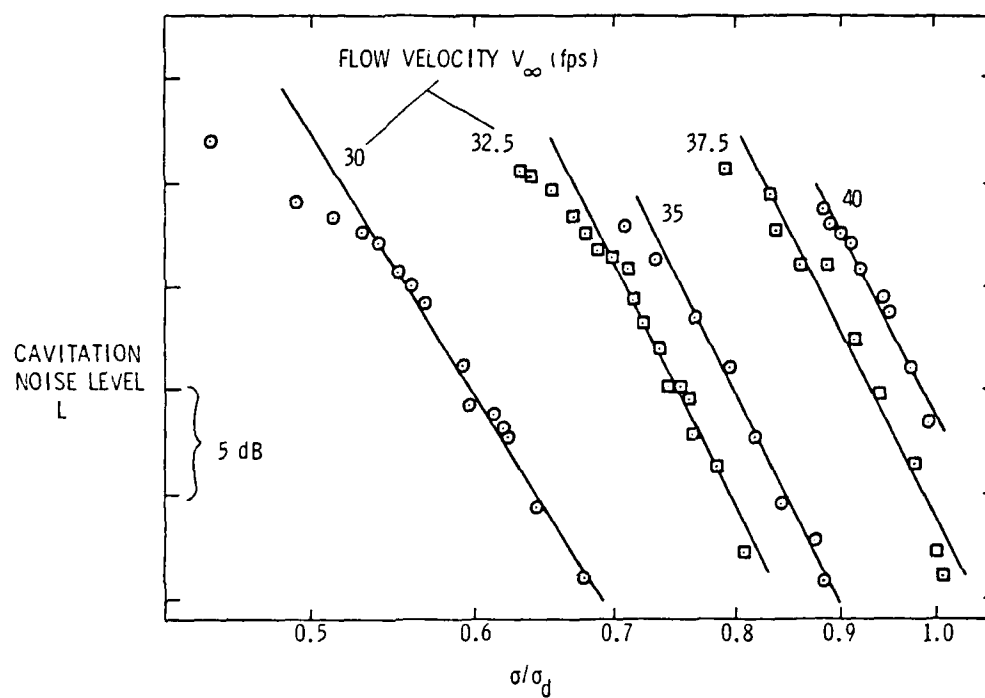


Figure 28. Cavitation Noise Level Versus σ/σ_d at Velocities from $V_\infty = 30$ to 40 fps

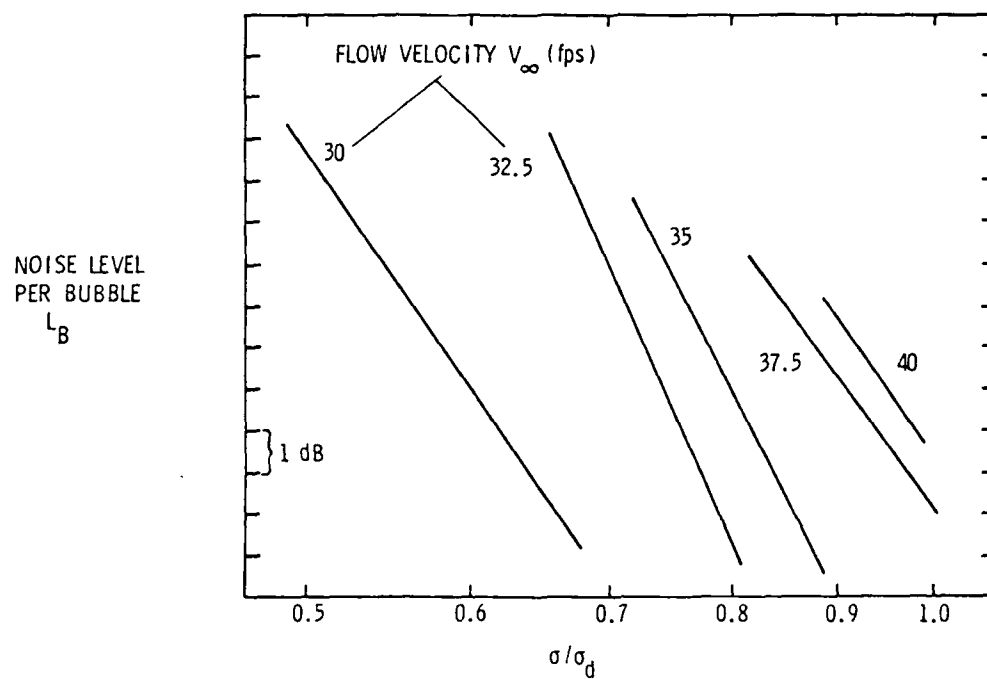


Figure 29. Noise Level Per Bubble Versus σ/σ_d at Velocities from $V_\infty = 30$ to 40 fps

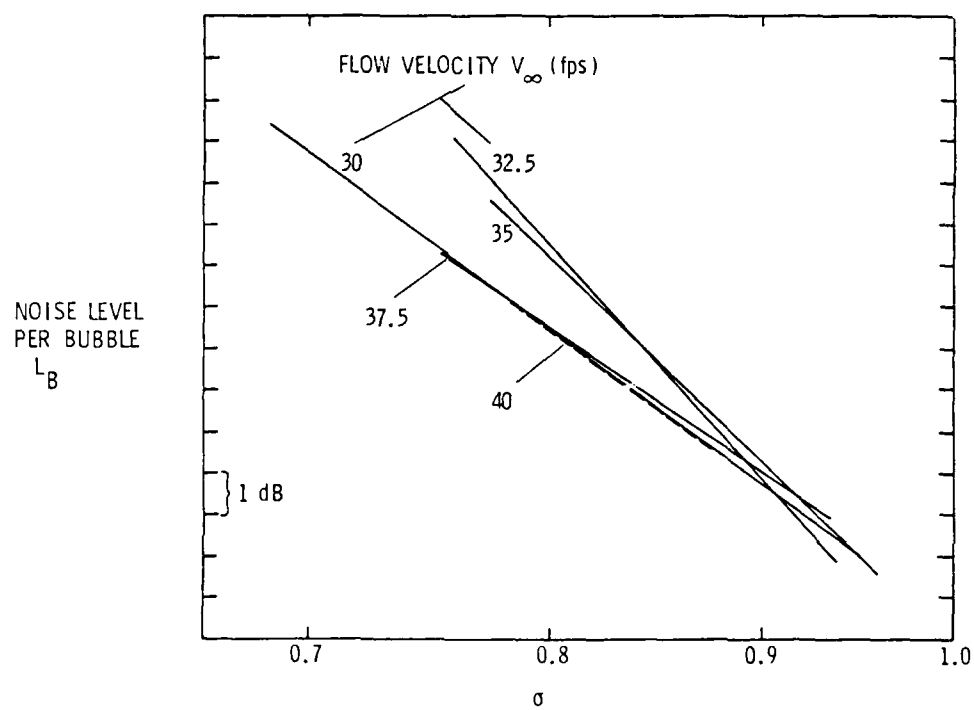


Figure 30. Noise Level Per Bubble Versus σ at Velocities from $V_\infty = 30$ to 40 fps

TABLE 2

FUNCTIONAL RELATIONSHIPS DEDUCED FOR
THE DEPENDENCE OF N , L AND L_B ON σ

Each dependence assumes the form σ^k for each specified velocity.

	<u>V_∞ (fps)</u>	<u>k</u>
i) Number of noise bursts per second; N	30.0	- 8.8
	32.5	- 8.7
$N \sim \sigma^k$	35.0	-10.5
	37.5	-12.7
	40.0	<u>-12.1</u>
average:		-10.6
ii) Noise level; L	30.0	-16.1
	32.5	-19.8
$L \sim \sigma^k$	35.0	-20.2
	37.5	-19.5
	40.0	<u>-19.4</u>
average:		-19.0
iii) Noise level per bubble; L_B	30.0	- 7.3
	32.5	-11.1
$L_B \sim \sigma^k$	35.0	- 9.7
	37.5	- 6.8
	40.0	<u>- 7.3</u>
average:		- 8.4

Figure 28 displays the results of the cavitation noise L plotted in decibels as a function of σ/σ_d . Again, a simple exponential relationship is seen to exist, and these functions are listed in Table 2. On average, the relationship is $L \sim \sigma^{-19.0}$. Notice how the data at low pressures break away from the trend set by the rest of the data. This happens at each of the velocities. However, this tendency is also hinted at in Figure 27. The implication is that cavitation bubble formation begins to level off shortly before the transition to an attached cavity.

Finally, Figure 29 presents the plot of the amount of noise generated per bubble as a function of σ/σ_d . These curves were calculated by subtracting the curves in Figure 27 from those in Figure 28, which yield an average noise per bubble $L_B \sim \sigma^{-8.4}$. Again, the functional relationships appear in Table 2. After removing the dependence on σ_d , the data reduce to the family of curves shown in Figure 30. Evidently, the acoustic energy seems to be essentially independent of velocity while maintaining the same exponential dependence on σ .

Using a Celesco LC-10 hydrophone mounted in a small parabolic plexiglass reflection disk on the test section window, spectra of the cavitation noise were measured with a Spectral Dynamics SD-360 FFT processor after high-pass filtering at 10 kHz. Calibration of the receiving LC-10 was accomplished using another LC-10 as a source which was located adjacent to the region on the model where cavitation noise is generated. Shown in Figure 31 is the free-field transmitting response of the source LC-10 due to a white noise excitation. This was obtained using gated tone bursts in a tank to avoid reverberation.

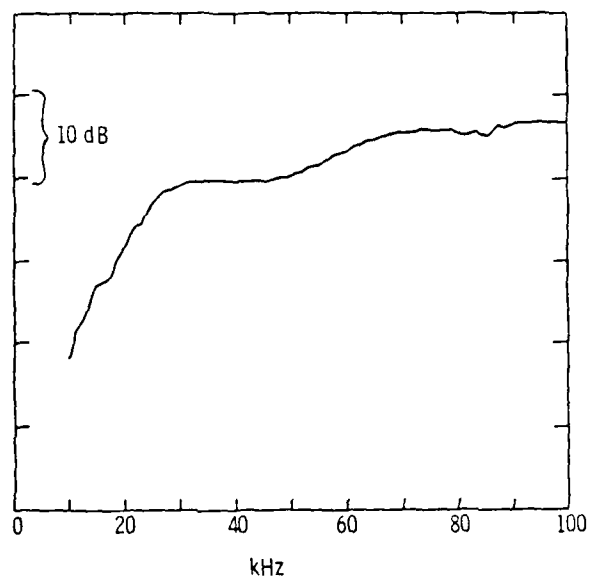


Figure 31. LC-10 Free-Field Transmitting Response

By driving this source with three volts rms of electrical white noise, the response of the receiving LC-10 hydrophone is deduced by correcting the resulting output spectrum using Figure 31. Thus, the spectrum shown in Figure 32 is the response that would be expected from the receiver due to true acoustic white noise being generated at a point on the surface of the model. As a consequence of the test section geometry which includes the presence of the model and the effect of the windows, a multitude of resonances can be expected. Coupled with the fact that the noise source is displaced off axis by almost two inches and is adjacent to a hard reflecting surface, i.e., the model, it is virtually impossible to conduct a thorough modal analysis of the system. A calculation of the zeroth order radial modes in a 12-inch diameter cylinder shows resonances occurring at approximately integer multiples of 5 kHz. Hence, it is possible that these resonances at 35 and 40 kHz are responsible for the large double peak located at those frequencies in Figure 32. It becomes increasingly more difficult to make such analyses at higher frequencies.

Cavitation noise at all velocities from 25 to 40 fps was observed to produce noise spectra having identical shapes between 10 and 100 kHz. Frequencies below 10 kHz were not studied because of an inability to calibrate in that range. Additionally, near-field effects also make the validity of measurements below 10 kHz questionable. The wavelength of sound in water at 10 kHz is already about 6 inches, which is the distance from the noise source to the hydrophone.

In Figure 33 are displayed typical spectra obtained at 30 fps. These records represent noise spectra, which have not been corrected yet for tunnel effects and hydrophone response characteristics, taken

AD-A099 409

PENNSYLVANIA STATE UNIV UNIVERSITY PARK APPLIED RESE--ETC F/G 20/1
TRAVELLING BUBBLE CAVITATION AND RESULTING NOISE.(U)
MAR 81 M F HAMILTON N00024-79-C-6043
UNCLASSIFIED ARL/PSU/TM-81-76 NL

212

AD-A099 409

END
DATE
FILMED
6-81
DTIC

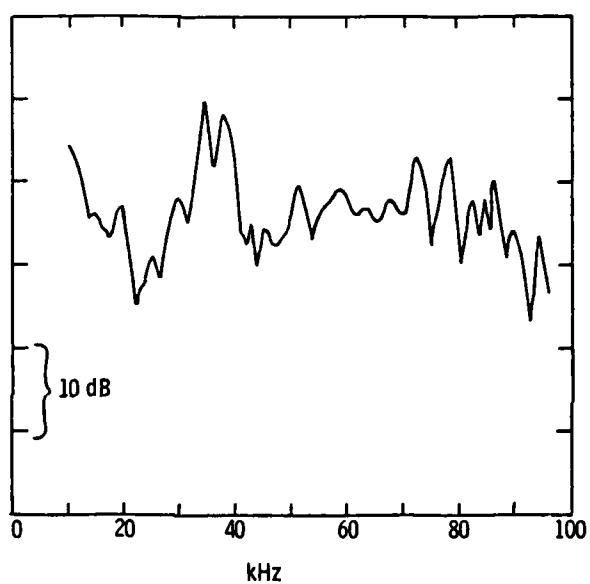


Figure 32. Receiver Response to Omnidirectional White Noise Source Located Adjacent to Model in Test Section

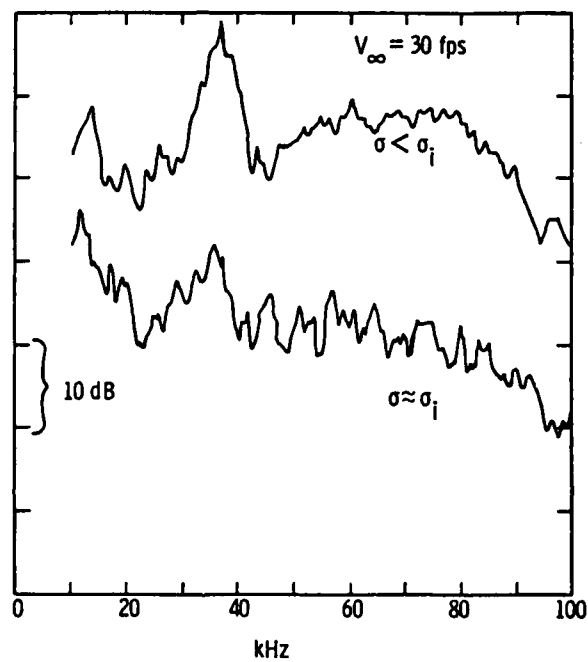


Figure 33. Raw Voltage Spectra from Receiver, Uncorrected for Receiver Response to White Noise, of Incipient and Well Developed Travelling Bubble Cavitation at $V_\infty = 30 \text{ fps}$

at a pressure near inception and again at a lower pressure supporting developed travelling bubble cavitation. The purpose of this figure is to illustrate that, even if cavitation noise near inception is taken to be the background level, the cavitation noise of interest is at least 10 dB above background, and consequently the background noise may be ignored.

To arrive at a spectrum representing the noise in an environment free from effects due to the water tunnel and hydrophone response characteristics, the upper curve in Figure 33 is corrected using Figure 32 to yield the spectrum in Figure 34. It is believed that, in addition to the bandwidth characteristics of the SD-360, the resonances observed in this curve may be attributed to the fact that the source used for calibration did not adequately represent the cavitation noise in terms of location. In particular, the fact that cavitation encompasses a circumferential strip around the model might, when considered to be a distributed source, tend to smear the resonance peaks together. It is interesting to note that the lower curve in Figure 33, which was obtained before cavitation became the significant source, shows many of the fine structure resonances that appear in Figure 32. That the upper curve of Figure 33 does not display this same definition of resonance peaks seems to reflect the problem of calibration source location.

In view of this argument, it is reasonable to assume that the resonance structure observed in Figure 34 is an artificial result created by both the calibration technique and the limited bandwidth resolution of the FFT processor. Hence, averaging was performed on

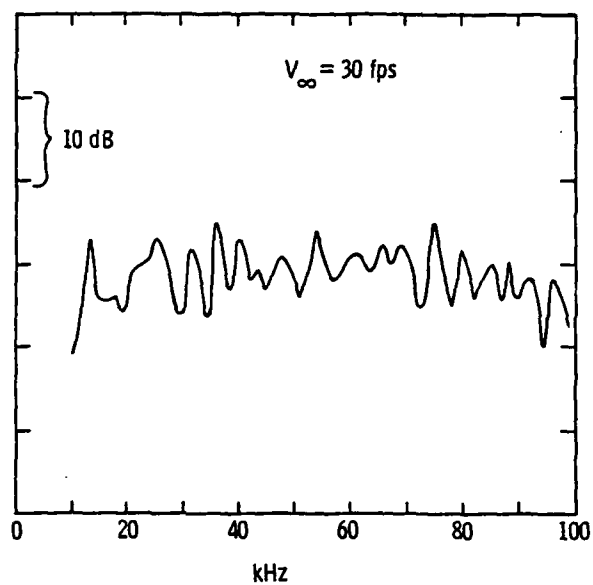


Figure 34. Cavitation Noise Spectrum After Correction
for Receiver Response to White Noise,
 $V_\infty = 30 \text{ fps}$

Figure 34 to yield the final result displayed in Figure 35. This result shows a relatively flat spectrum with the possible hint of roll-off at both the lower and upper ends.

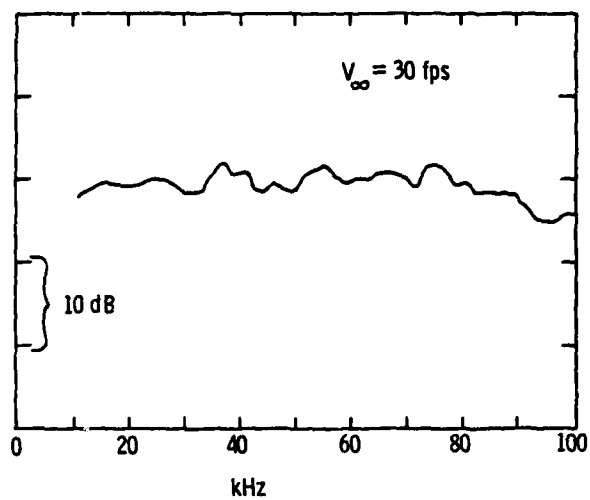


Figure 35. Smoothed Cavitation Noise Spectrum After Correction for Receiver Response to White Noise, $V_\infty = 30 \text{ fps}$

CHAPTER V

SUMMARY

5.1 Discussion

No attempt was made in this investigation to calculate absolute sound pressure levels generated by travelling bubble cavitation. Instead, the emphasis was upon determining how the noise level varied as a function of the free stream velocity and pressure in the test section of the water tunnel. In summary, it was found that the noise level per bubble was roughly proportional to σ^{-8} at each velocity, whereas it was approximately independent of the flow velocity when σ was constant. These results were obtained for a range of velocities from 30 to 40 fps in water having an average air content of 10 ppm.

It is interesting to compare predictions suggested by the single bubble noise theories with the results from this study. Rayleigh's incompressible theory is perhaps both the simplest and most often quoted, and thus serves as a good starting point. His analysis yields a pressure pulse having an envelope given by $t^{-4/5}$. Using bubbles created by spark gaps, Mellen (7) in 1955 measured the resulting pressure waves and found their amplitudes to indeed behave as $t^{-4/5}$ for most of the collapse stage. However, his initial bubble radii R_M were between 10 and 20 mm, which are much larger than the bubbles encountered in this investigation. It is nevertheless significant that the incompressible theory seems to correctly model the collapse up until the final stages where compressibility and possibly noncondensable gas contents become important.

If the energy density of that pressure pulse, given by $S(f)$ in Equation (27), is used in conjunction with the equation for the maximum bubble radius R_M given by Equation (13), the following functional relationship with σ results:

$$S \sim (\bar{C}_p + \sigma)^{9/5} (C'_p + \sigma)^{6/5} . \quad (31)$$

Here, \bar{C}_p represents the average pressure experienced by the bubble in the region $P < P_v$, and C'_p represents the local pressure where collapse occurs. For simplicity, it is easiest to take $\bar{C}_p = C_{p_{\min}}$, which in this case yields $\bar{C}_p = -1$. From Figures 16, 17, and 18 along with Figure 9, it can be seen that a reasonable value to represent the pressure forcing collapse might be $C'_p = -1/3$. Thus, Equation (31) becomes:

$$S \sim (1 - \sigma)^{9/5} (\sigma - 1/3)^{6/5} . \quad (32)$$

The logarithm of Equation (32) is plotted against the logarithm of σ in Figure 36. On that same graph is plotted a line illustrating a relationship of the type $S \sim \sigma^{-8.4}$, which is the mean dependence on σ suggested by Figure 30. Note that the approximation to the $\sigma^{-8.4}$ line is excellent between $\sigma = 0.8$ and $\sigma = 0.9$, and that is exactly the range in which most of the data were taken. However, the apparent agreement with incompressible theory stops there, because Equation (27) also shows a dependence on velocity as $V_\infty^{2.4}$ for constant σ which cannot be ignored. That, of course, seems to contradict the results of this study.

Comparisons made with the spectral response also do not seem to be consistent with incompressible theory. Fitzpatrick and Strasberg (9)

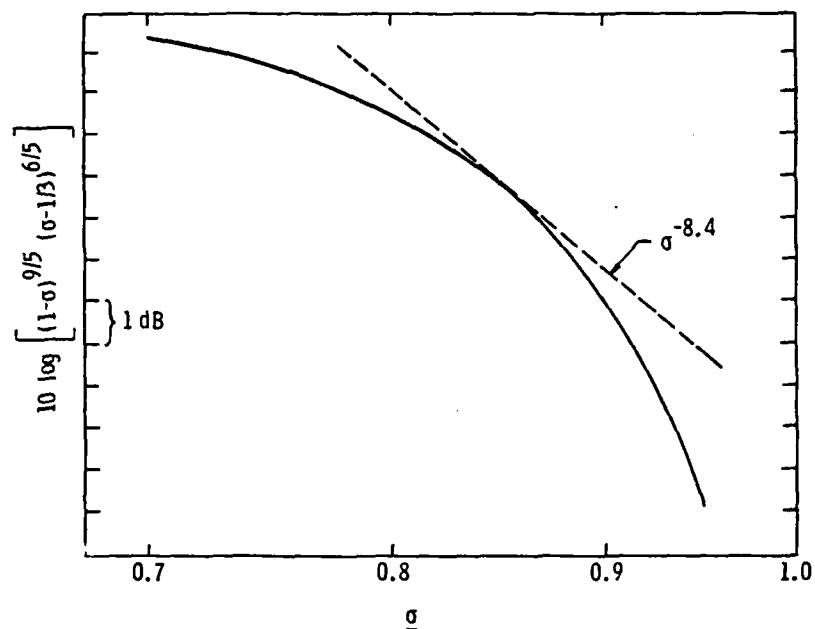


Figure 36. Comparison of Experimental Results with Incompressible Theory for Cavitation Noise

discuss a roll-off following a peak in the spectrum occurring at $f \approx 1/\tau_c$, with τ_c the collapse time of the bubble. From analysis of the high-speed films and Figures 15 through 18, collapse times were observed to be in the range between 1 and 2 msec. This implies the location of a spectral peak between 500 and 1000 Hz, well below the cutoff of the 10 kHz filter used in this investigation. Incompressible theory predicts a $f^{-2/5}$ dependence at high frequencies, or in the 10 to 100 kHz range reported here. As seen in Figure 35, an essentially flat spectrum was observed in that range.

Mellen (10), and more recently, Blake et al. (19) reported a f^{-2} trend at frequencies immediately above the peak near $f \approx 1/\tau$. Interestingly, the spectra obtained by Blake et al. appear to gently rise to a new plateau between 10 and 100 kHz before starting to roll off again, very similar to that depicted in Figure 35. Mellen also observed a plateau in this region. In another study, Barker (23) also reported for incipient cavitation a spectral plateau between 10 and 100 kHz which possessed the same shape as that in Figure 35. An important result from that test came from a comparison of the spectra due to incipient cavitation at a constant σ for velocities of 25, 30 and 35 fps. In the frequency range between 10 and 100 kHz, the spectra were identical, as predicted by Figure 30.

Barker warned against generalizing from trends observed in any limited frequency region. For instance, in the same test that showed no velocity dependence between 10 and 100 kHz, he found the total acoustic energy in the 1 to 10 kHz band to vary as V_∞^6 . His data also suggested some dependence on velocity above 150 kHz. Hence, although this investigation showed no significant velocity dependence above

10 kHz, one cannot infer that the total acoustic energy summed over all frequencies will also remain constant with velocity.

The high frequency spectral plateau implies the existence of shock waves with spectra described by formulas such as Equation (18). Both shock wave theories by Baiter (13) and Esipov and Naugol'nykh (14) include the effects of noncondensable gases trapped within the bubble, as discussed in Section 2.1. Using estimates of R_M from Figures 16 through 18 and assuming a maximum noncondensable gas pressure P_G to be around the vapor pressure of water, values for the roll-off frequency are calculated for the two theories. Baiter's theory for incompressible fluids shows a roll-off at about 300 kHz, while the compressible analysis of Esipov and Naugol'nykh shows cutoff frequencies between 50 and 100 kHz for velocities between 25 and 40 fps.

That the lower roll-off is given by the compressible theory appears reasonable considering that a portion of the collapse energy will be imparted toward compressing, or actually rarefying, the fluid. A less violent collapse yields a weaker shock front and consequently, a smaller contribution of high frequency components. Both theories predict an increase in the roll-off frequency as P_G is reduced. Less noncondensable gas pressure means less cushioning of the bubble collapse, creating a steeper shock front that will generate more high frequency energy. Hence, a slight reduction in P_G will push the cutoff frequency for the compressible theory above 100 kHz, such that a flat spectrum will coincide with the observed behavior.

If most of the acoustic energy is taken to be below the cutoff frequency, it was shown in Section 2.2 that both shock wave theories

predict the sound power to vary as R_M^4 . In performing an analysis similar to that done for Rayleigh's incompressible theory, one indeed finds that a σ^{-8} trend exists in the neighborhood of $\sigma = 0.8$ when either Equation (13) or (14) is used for R_M . However, those trends show radically different functional relationships away from $\sigma = 0.8$, which perhaps discredits this method of interpreting these equations more than the equations themselves. On the other hand, assuming R_M to be a function of σ alone and holding it constant, the theory does correctly predict that the noise level will not increase simply as a function of velocity.

More than anything, this discussion has illustrated the need for information on the behavior of R_M as a function of velocity and pressure. Attempts were made to investigate this problem using the video tapes taken of cavitation, but no meaningful results came from that study. One reason was that the projection of the bubbles on the television screen was not always indicative of the bubble volume from which R_M is derived. For instance, when interpreting Figures 15 through 18, it was assumed that the plotted bubble diameters which represent the dimension of the circular projection of bubbles were in fact about three times that of the dimension perpendicular to the field of view. This appeared to be approximately the ratio observed in the high-speed films where the bubbles could be seen in profile, as in Figure 11. Since this ratio is itself a function of σ , which approaches 1:1 for small bubbles, i.e., high pressure, it became virtually impossible to correctly interpret any trends observed on the tapes.

It is noteworthy to look at some of the bubble dynamics formulas of Section 2.1. Compared with data from the high-speed films along with Figures 16 through 18, the measured values of R_M were found to be between 2 and 4 times larger than the values calculated using Equation (13). Even Equation (14), which is intended to allow for inertial growth, only increased the calculated values by 10 to 20 percent. Blake et al. (19) made similar calculations for their bubbles which were generated along a hydrofoil, and found Equation (13) to overestimate their data by about 20 percent.

It is certainly true that cavitation on different bodies carried out in different facilities may be subject to some very different parameters. On the other hand, it is essentially the effects of the pressure field which govern bubble dynamics. Thus, it is desirable to find formulas that adequately predict trends in bubble behavior, such as for R_M , without resorting to methods like the numerical solution of the Rayleigh-Plesset equation. Simply because the values that were calculated did not correspond to the correct magnitude of R_M , this does not discount the possibility that the formula might still describe the proper functional dependence on σ .

Calculated values for the collapse time using Equation (28) underestimated the observed times by a factor of anywhere from 2 to 4. Similarly, Blake et al. also found the calculations to produce values that were less than their data for collapse times, but only by about 15 percent. It is not surprising to find that the predicted collapse times are too short, owing to the fact that the equation is derived under the assumptions that the liquid is incompressible and there is no noncondensable gas in the bubble. Including either of

those effects serves to retard the rate of collapse. Investigation of these and similar aspects of bubble dynamics has been done more extensively elsewhere (2, 24).

Consideration was also given to determining an appropriate dimensionless quantity that would represent the functional dependence on σ . Recalling Figures 27 and 28, it is seen that σ was normalized by the desinent cavitation number σ_d . Although this normalization spread out the data for clearer presentation, it was initially thought that σ/σ_d , or even σ/σ_i , would serve as the appropriate scaling factor. As can be seen from Figure 30, merely plotting the data against σ was sufficient to collapse the results.

This is somewhat surprising when one recalls the inception curves of Figure 10. Since the data in Figures 27 and 28 represent the entire range of σ at each velocity where the noise data was meaningful, they essentially define the pressure region of significant travelling bubble cavitation noise. By inspection, it can be seen that Figures 27 and 28 will collapse in the same fashion as Figure 29. Thus, the value of σ at which significant bubble activity occurs is roughly the same regardless of the velocity. The possible exception is at 40 fps, but this velocity was on the borderline where the acquisition of data became extremely difficult.

It would seem that both the amount of noise and number of events should be related to the value of σ where cavitation begins. That this is not the case might be a reflection of the problem involved with determining σ_i and σ_d , which was itself a subject of discussion earlier in this report. Assuming Figure 10 to be reasonably accurate,

one might consider searching for an appropriate constant factor by which σ might be scaled. A likely candidate for this function is the constant $-C_{p_{\min}}$.

One reason for choosing $-C_{p_{\min}}$ is that this parameter, under certain assumptions, determines theoretically where vaporous cavitation should incept, i.e., when $\sigma = -C_{p_{\min}}$. This was discussed in Section 3.5. Also, even though $C_{p_{\min}}$ is constant for the range of pressure encountered in this investigation, there are many situations where this is not the case. For example, hemispherical noses exhibit a variable $C_{p_{\min}}$ as a function of the Reynolds number. Thus, the rationale for choosing σ_i or σ_d as a normalization factor seems sensible if those parameters can be determined accurately in relation to cavitation noise. Methods for doing this are discussed in Appendix B. However, since in theory $\sigma_i = -C_{p_{\min}}$ for vaporous cavitation, the results of this study seem to recommend a scaling factor of the form $-(\sigma/C_{p_{\min}})$.

Finally, it is important to consider how the results from this investigation might scale with model size. The effect of changing the model size will be to change the scale of the abscissa in the C_p curve shown in Figure 9. Assuming the maximum bubble size R_M to be proportional to the length of time that the bubble experiences a pressure less than P_v , R_M should then scale with model size for a given velocity. This change in R_M may, of course, be offset by scaling V_∞ the same as the model size, thus adjusting the time spent by the bubble in the low pressure region to match the unscaled case. If R_M is allowed to vary with the model size by maintaining a constant flow velocity, a shift might be expected in the frequency

spectrum. Both the linear and shock wave theories predict high-frequency cutoffs that are inversely proportional to R_M . If it is assumed that R_M does not become significantly larger than the values encountered in this investigation, then the functional dependence of the noise per bubble on σ should also be near σ^{-8} for pressure distributions resembling that in Figure 9.

5.2 Conclusion

In claiming that cavitation bubbles emit sound having energy that varies roughly as σ^{-8} and not at all with V_∞ , acoustic energy in the region below 10 kHz has been ignored. This is because such facilities as various water tunnels generate so much low frequency noise that taking data in this region is extremely difficult, not to mention calibration problems and near-field effects. Hence, it is not certain whether the observed trends are valid at the lower frequencies where the noise level can be 20 dB higher than that observed above 10 kHz. Since the remaining acoustic energy above 10 kHz extends as a flat spectrum to at least 100 kHz, this portion is by no means insignificant in relation to that at low frequencies. Thus, although the trends that were observed do not represent the entire spectrum, they should be highly indicative of what might be expected.

No single analytical noise theory was capable of adequately describing the trends observed in this investigation. However, different theoretical models might be suitable for application to various regions of the energy spectrum. For instance, the flat spectral response above 10 kHz seems to indicate the presence of a strong shock wave component. Both shock wave theories that were considered predict

both this type of spectral behavior as well as the lack of any dependence on velocity. On the other hand, the incompressible analysis, which does not account for high frequency energy, correctly describes how the total noise energy depends on pressure. Additionally, this theory predicts a dependence on velocity. Other studies have also suggested a velocity dependence, particularly below 10 kHz. Thus, one might employ the incompressible theory when analyzing low frequency noise energy, up to a point where it becomes appropriate to describe the higher frequency energy by a shock wave model.

Although the amount of noise being emitted by a single bubble might be known, it could be more than a matter of simply multiplying that quantity by the number of cavitation bubbles to arrive at the total noise output. This was illustrated when some rebounding bubbles were observed to emit almost as much sound as the initial collapse. Hence, one bubble may generate a number of acoustic pulses having roughly equivalent energy. It was at low air content where this rebound phenomenon was found to be most prevalent, whereas one might be able to ignore it at higher air contents.

Finally, it is borne out in this study how important the maximum bubble radius is as a parameter in all of the noise theories. An experimental study of how this parameter depends on flow variables is strongly recommended as an area for future research. Also of importance is a better understanding of the noncondensable gases which cushion bubble collapse. Ultimately, it is desirable to deduce analytical theories from data to describe these quantities, as opposed to resorting

to numerical solutions of the nonlinear differential equations describing bubble dynamics to analyze each new situation. Only then can one hope to use single bubble theories confidently for modeling cavitation noise.

REFERENCES

1. Knapp, R. T., Daily, J. W., and Hammitt, F. G. Cavitation, New York: McGraw-Hill, 1970.
2. Hammitt, F. G. Cavitation and Multiphase Flow Phenemona, New York: McGraw-Hill, 1980.
3. Besant, W. H. Hydrostatics and Hydrodynamics, Art. 158, London: Cambridge University Press, 1859.
4. Rayleigh, Lord (Strutt, J. W.). "On the Pressure Developed in a Liquid During the Collapse of a Spherical Cavity," Philosophical Magazine, Vol. 34, pp. 94-98, August 1917.
5. Kirkwood, J. G., and Bethe, H. A. "The Pressure Wave Produced by an Underwater Explosion," Office of Research and Development, Report 588, 1942.
6. Gilmore, F. R. "The Growth and Collapse of a Spherical Bubble in a Viscous Compressible Liquid," California Institute of Technology, Report 26-4, 1952.
7. Mellen, R. H. "An Experimental Study of the Collapse of a Spherical Cavity in Water," Underwater Sound Laboratory, Report No. 279, October 3, 1955.
8. Mellen, R. H. "Spherical Pressure Waves of Finite Amplitude from Collapsing Cavities," Underwater Sound Laboratory, Report No. 326, September 17, 1956.
9. Fitzpatrick, H. M., and Strasberg, M. "Hydrodynamic Sources of Sound," 1st Symposium on Naval Hydrodynamics, Publication 515, September, 1956.
10. Mellen, R. H. "Ultrasonic Spectrum of Cavitation Noise in Water," Journal of the Acoustical Society of America, Vol. 26, pp. 356-360, May, 1954.
11. Hickling, R., and Plesset, M. S. "Collapse and Rebound of a Spherical Bubble in Water," Physics of Fluids, Vol. 7, pp. 7-14, 1964.
12. Ivany, R. D., and Hammitt, F. G. "Cavitation Bubble Collapse in Viscous, Compressible Liquids--Numerical Analysis," Journal of Basic Engineering, Transactions of ASME, Vol. 87, Series D, pp. 977-985, 1965.

13. Baiter, J. J. "Aspects of Cavitation Noise," Proceedings of Symposium on High Powered Propulsion of Ships, Wageningen, The Netherlands, December, 1974.
14. Esipov, I. B., and Naugol'nykh, K. A. "Collapse of a Bubble in a Compressible Liquid," Soviet Physics-Acoustics, Vol. 19, pp. 187-188, 1973.
15. Akulichev, V. A., and Ol'shevskii, V. A., "Relationship Between the Statistical Characteristics of Acoustic and Cavitation Noise," Soviet Physics-Acoustics, Vol. 14, pp. 22-26, 1968.
16. Il'ichev, V. I. "Statistical Model of the Onset of Hydrodynamic Cavitation Noise," Sixth All-Union Acoustic Conference, Collected Papers, Moscow, 1968.
17. Lyamshev, L. M. "On the Theory of Hydrodynamic Cavitation Noise," Soviet Physics-Acoustics, Vol. 15, pp. 494-498, 1970.
18. Morozov, V. P. "Cavitation Noise as a Train of Sound Pulses Generated at Random Times," Soviet Physics-Acoustics, Vol. 14, pp. 361-365, 1969.
19. Blake, W. K., Wolpert, M. J., Geib, F. E., and Wang, H. T. "Effects of Boundary-Layer Development on Cavitation Noise and Inception on a Hydrofoil," David W. Taylor Naval Ship Research and Development Center, Report 76-0051, December, 1976.
20. Hentschel, W. "Acoustic and Optical Investigation on the Dynamics of Holographically Generated Cavitation Bubble Systems," Ph.D. thesis, Third Physical Institute of the Universität, Göttingen, 1979.
21. Fitzpatrick, H. M. "Cavitation Noise," 2nd Symposium on Naval Hydrodynamics, ACR-38, August, 1958.
22. Schiebe, F. R. "Measurement of the Cavitation Susceptibility of Water Using Standard Bodies," St. Anthony Falls Hydraulic Laboratory, University of Minnesota, Report No. 118, February, 1972.
23. Barker, S. J. "Measurements of Radiated Noise in the Caltech High-Speed Water Tunnel - Part II: Radiated Noise from Cavitating Hydrofoils," Graduate Aeronautical Laboratories, California Institute of Technology, March, 1975.
24. Plesset, M. S. "The Dynamics of Cavitation Bubbles," Journal of Applied Mechanics, Vol. 16, Transactions of ASME, Vol. 71, pp. 277-282, 1949.
25. Schiebe, F. R. "Cavitation Occurrence Counting - A New Technique in Inception Research," Cavitation Forum Paper, ASME Annual Meeting, 1966.

26. Brockett, T. "Some Environmental Effects on Headform Cavitation Inception," David W. Taylor Naval Ship Research and Development Center, Report 3974, October, 1972.
27. Keller, A. P. "The Influence of the Cavitating Nucleus on Cavitation Inception, Investigated with a Light Counting Method," Journal of Basic Engineering, ASME, pp. 917-925, December, 1972.
28. Billet, M. L., and Gates, E. M. "A Comparison of Two Optical Techniques for Measuring Cavitation Nuclei," International Symposium on Cavitation Inception, ASME, New York, December, 1979.

APPENDIX A

RAYLEIGH THEORY OF BUBBLE COLLAPSE

Rayleigh (4) derived a formula for the bubble wall velocity during collapse by equating the total kinetic energy:

$$\frac{1}{2} \rho \int_R^{\infty} u^2 \cdot 4\pi r^2 dr = 2\pi \rho \dot{R}^2 R^3 ,$$

where use was made of $u = (R/r)^2 \dot{R}$, and the total work done:

$$\frac{4}{3} \pi (P - P_v) (R_o^3 - R^3)$$

to arrive at:

$$\dot{R} = \left[\frac{2}{3\rho} (P - P_v) \left(\frac{R_o^3}{R^3} - 1 \right) \right]^{1/2} . \quad (A1)$$

The variables are as defined in Section 2.1 with R_o the initial value of R . Note that Equation (A1) will reduce to Equation (8) for bubble growth if $R \gg R_o$. In this case, for a collapsing bubble, introducing C_p and σ while assuming R to be much less than the initial radius $R_o = R_M$ yields:

$$\dot{R} = v_{\infty} \left[\frac{1}{3} (C_p + \sigma) \right]^{1/2} \left(\frac{R_M}{R} \right)^{3/2} .$$

Integration of the above relation results in an asymptotic relation for R as a function of time:

$$R \sim [v_{\infty}^2 R_M^3 (C_p + \sigma)]^{1/5} t^{2/5} .$$

Substitution into Equation (6) yields for the acoustic pulse:

$$p(r,t) \sim \left(\frac{\rho}{r}\right) [V_{\infty}^2 R_M^3 (C_p + \sigma)]^{3/5} t^{-4/5} .$$

Since $p(r,t)$ exists only for positive t , the Fourier transform of $p(r,t)$ may be determined by analogy with its Laplace transform. Finally, the energy density spectrum of $p(r,t)$, found by squaring its Fourier transform, is:

$$S(f) \sim \left(\frac{\rho}{r}\right)^2 [V^2 R_M^3 (C_p + \sigma)]^{6/5} f^{-2/5} .$$

APPENDIX B

ACOUSTIC DETERMINATION OF CAVITATION INCEPTION

Using cavitation noise to call inception of travelling bubble cavitation was first described by Schiebe (25) in 1966. His method entailed counting the noise bursts produced by the collapsing cavitation bubbles and then deciding upon a certain rate of occurrence as being the point of inception. Various ways of counting these bursts are described in detail in Appendix C.

Since the nature of the cavitation noise will change as different headforms are used, the appropriate rate of occurrence for inception must be determined each time by comparison with visual calls. Although this might seem to defeat the purpose of the procedure, once a particular rate has been chosen, the quantitative measurement should provide a more convenient way to monitor any change in the inception pressure. The problem encountered in this investigation was that the cavitation noise bursts as seen on an oscilloscope looked different depending on the flow velocity.

At the higher velocities, for instance between 35 and 40 fps, the noise bursts near inception were both well defined and adequately spaced for counting. Reliable results could be obtained in this range because the count increased slowly near the point of inception. At velocities between 25 and 30 fps, many small noise bursts would begin to simultaneously rise above the background noise. The additional pulses encountered near inception at these low velocities probably resulted from gaseous cavitation which becomes prevalent at low pressures. These bursts all tended to be approximately the same size,

so when they grew large enough to be above some threshold where they were counted, that count would change discontinuously to a much larger value. Where that change occurred was extremely sensitive to the level of the threshold. This problem produced erratic results at the lower velocities, along with making it very difficult to set an appropriate threshold and a meaningful rate.

A reasonable alternative to this method seemed to be a measurement of the rms noise level. Some level of, say, 3 or 6 dB above the background noise level might be a useful way of defining inception. This technique showed difficulties in ranges that were the reverse of the previous method. At the low velocities, the gradual appearance of all the noise bursts produced a smooth change in the rms noise level. This made it easy to record the pressure where a particular noise level was exceeded. Bursts occurring at higher velocities were larger and contained more energy. As a result, 10 dB excursions of the voltmeter were common near inception, even with reasonable integration times. Again, these inconsistencies when making noise measurements near inception at different velocities were probably due in part to effects of gaseous cavitation at low pressures. It was thus virtually impossible to employ this method at the higher velocities.

These techniques were tried because, considering that this is an investigation of cavitation noise, it seemed appropriate to define the point at which cavitation starts in terms of that noise. Visual calls of inception will vary from one observer to another, and can only be described in a qualitative manner. Furthermore, it is often difficult to discriminate between natural air bubbles in the free stream and bubbles caused by cavitation when the pressure is near

inception. All things considered, visual calls of inception still seemed to be the most reliable for the purposes of this investigation.

APPENDIX C

METHODS OF COUNTING CAVITATION NOISE BURSTS

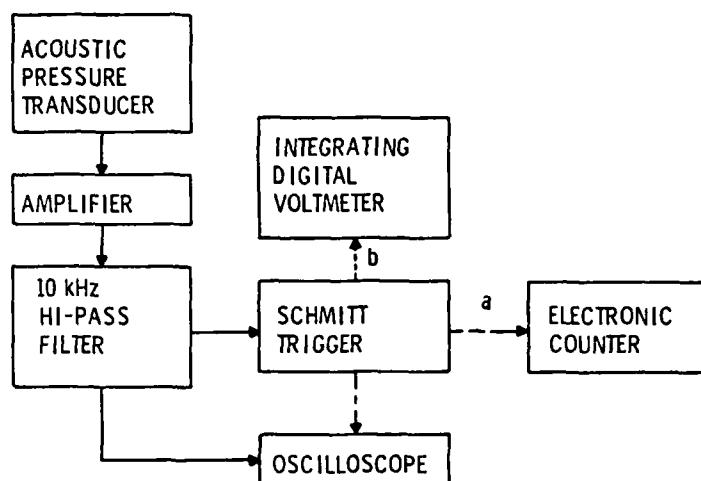
This section describes methods by which it was attempted to measure the rate at which sound bursts were being emitted from the cavitating headform. It should be pointed out that even an accurate count of these pulses might not correspond exactly to the number of bubbles that were collapsing. For instance, echoes might be counted as well as multiple pulses emitted by a single bubble. Also, some bubbles might collapse without being accompanied by any significant sound output. It was thus initially proposed that a count of the noise pulses be complemented with a measurement of the cavitation nuclei size distribution. This was to be done using the ARL/PSU laser light-scattering system to count the nuclei. A description of that system and the reasons why it was not used appears in Appendix D.

The cavitation noise pulses witnessed in this investigation seemed to be high frequency impulses that were followed by a resonance that was characteristic of the transducer being used. Consequently, the noise output appeared as a series of exponentially damped sinusoids, a typical example of which is shown in Figure 23. Although the initial impulse was of much greater amplitude than the ringing that followed, it was of such high frequency and short duration that conventional electronic counters would rarely detect it. Those devices are as likely to count the cycles that make up the ring from the transducer and produce meaningless results.

Brockett (26) discusses a method where a blanking pulse could be introduced to reject the remainder of each noise pulse after a counter has been triggered by the first cycle. This technique was being applied toward standardizing the point at which inception should be called. Problems are incurred as the cavitation becomes more active and the noise pulses begin to overlap each other. Hence, the blanking pulse will serve to reject incoming noise signals that occur too close to the burst just counted.

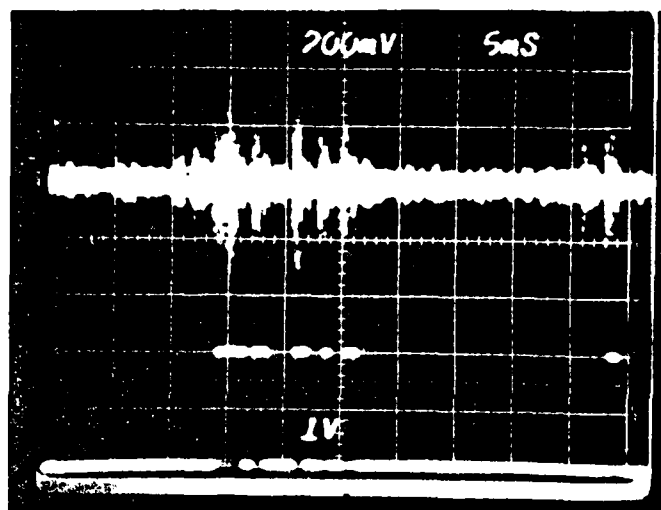
To solve that problem, an instrument made at ARL/PSU that operated much like a Schmitt trigger was employed. This device effectively monitored the amplitude of the envelope of each burst and compared that value with a variable threshold. When the envelope amplitude was above some set threshold, an output of 2.1 volts was seen at the output of the trigger, while 0.2 volts was seen at all other times. The signal from the output of the transducer was input directly to this device after being amplified and high-pass filtered. This setup is illustrated in Figure 37. A typical oscilloscope trace of the input and output signals at the trigger is shown in Figure 38a.

The threshold of the Schmitt trigger must be set low enough to compare with the noise bursts occurring slightly below the inception pressure. These bursts were somewhat smaller in magnitude than those occurring at lower pressures, yet must be counted to describe the entire range of cavitation that is of interest in this study. Ideally, each burst should correspond to a single rectangular pulse being generated by the trigger, the output of which was input to an electronic counter.

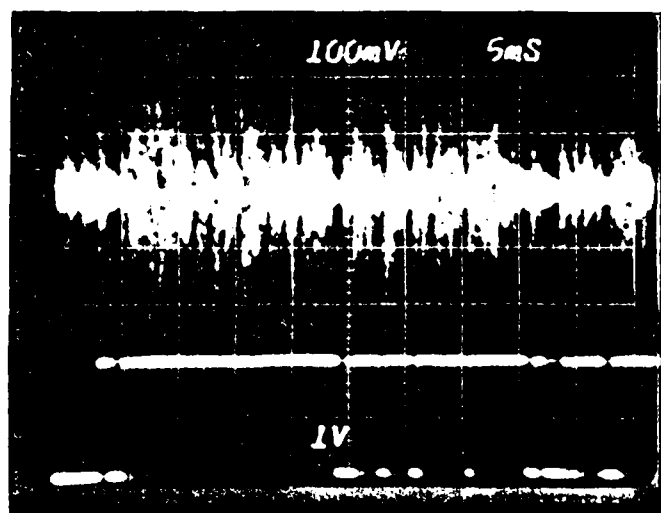


- a. ELECTRONIC COUNTER MONITORS THE NUMBER OF PULSES COMING FROM THE TRIGGER
- b. VOLTMETER CALCULATES AREA PER UNIT TIME UNDER PULSES COMING FROM THE TRIGGER

Figure 37. Schematic Diagram Depicting Setups Used to Count Cavitation Noise Bursts



(a)



(b)

Figure 38. Oscillographs Showing Cavitation Noise and Resulting Output from a Schmitt Trigger for (a) Limited and (b) Developed Travelling Bubble Cavitation

As the pressure was lowered and the bursts became larger and closer together, a problem was encountered that was similar to the one faced when using a blanking pulse. If two bursts overlapped in time such that the envelope decay of the first burst had not fallen below the trigger threshold by the time the second burst occurred, the trigger would not drop to the low voltage level. Consequently, the counter would register only one event because of seeing only one long pulse instead of two short pulses. Similarly, a whole train of closely spaced bursts might be counted as a single event. A photograph of this situation is shown in Figure 38b.

If the trigger threshold was raised enough to avoid this problem, many of the smaller bursts would not be counted, particularly at higher pressures. It did not seem possible to continuously alter the threshold level to accommodate the changing burst height and avoid overlap. Thus, this method could not yield reliable results over the desired range of operation.

Finally, it was decided to integrate the output level of the Schmitt trigger and not even use a counter. This was done by feeding the output from the trigger into an integrating digital voltmeter, as shown schematically in Figure 37. Instead of counting events, the display on the voltmeter gave an indication of the area defined by the noise burst envelopes. If the number of bursts per second increased by a certain factor, it was hoped that the integration would increase by the same factor. This would still provide sufficient information to determine how the noise per bubble depends upon pressure and velocity.

For this method to work, each rectangular pulse from the trigger must have roughly the same width, regardless of the shape of the burst. To achieve this goal, the threshold should now be set as low as possible. Assuming an exponentially shaped burst envelope, a higher threshold will produce a larger pulse width ratio for any two bursts having a fixed total height ratio. However, this restriction can be relaxed somewhat since the magnitude of the transducer ring did not seem to increase at the same rate as the initial spike from the sound pulse.

A new problem was now encountered while attempting to use this procedure. As the pressure was lowered, the background flow noise would often rise to levels comparable to those of the smaller noise bursts. Hence, the threshold could not discriminate against the unwanted noise and would result in an unintended increase of the integrated Schmitt trigger voltage. Although these smaller bursts may make negligible contributions to the total noise level while in the presence of larger bursts, they are certainly significant during periods of lesser bubble activity. Since the threshold level must remain constant throughout each test, extreme care had to be taken while setting that level.

The other difficulty with this method was that tests at different velocities can produce cavitation noise bursts that look completely different. For instance, higher velocities tended to have more clearly defined and more widely separated bursts than the lower velocities. To deduce any relations that apply to different velocities, it was important that the threshold level have consistent settings at each of those velocities. A level suitable at one velocity was often

totally unsuitable for another. Since the difference in the type of cavitation noise could only be described in a qualitative way, it became almost impossible to relate the data taken at different velocities due to the subjective setting of the threshold.

All of these methods described were attempts to devise an on-line system to count the cavitation noise bursts. Although fairly reliable results can be obtained for infrequent bubble collapses, further work is needed to cover a larger range of cavitation. At the present time, it seems that the best procedure is to tape record the entire cavitation process for later digitization on a computer. All of the noise bursts may then be counted by hand.

APPENDIX D

CAVITATION NUCLEI ANALYSIS USING
A LASER LIGHT-SCATTERING SYSTEM

It has long been thought that the cavitation phenomenon is strongly influenced by the presence of tiny air pockets, or cavitation nuclei, already present in the free stream. These nuclei are weak spots in the fluid that will grow to become larger bubbles upon entering a sufficiently low pressure region. Thus, it seems that an accurate account of the quantity and size distribution of the nuclei should be highly indicative of the nature of the cavitation that one might expect to observe.

A theory developed by Mie in 1909 showed that there exists a monotonic function relating the light scattered from a spherical particle in a direction perpendicular to the incident beam to the size of that particle. Based on this theory, a laser light-scattering system was assembled at ARL/PSU, similar to that designed by Keller (27), in which a laser beam passed through the test section of the water tunnel in a direction perpendicular to the flow. A photomultiplier then collected the scattered light from particles passing through a control volume determined by the size of the laser beam and the aperture defining the line of sight of the photomultiplier. The signal from the photomultiplier underwent some processing before being input to a pulse-height analyzer. A diagram of this system is illustrated in Figure 39, and a photograph of the pulses due to the light scattering from particles passing through the control volume is

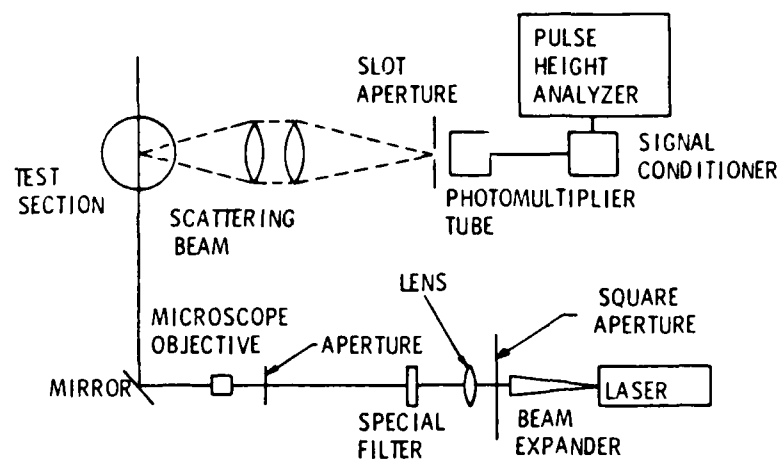


Figure 39. Schematic Arrangement of Laser Light-Scattering System

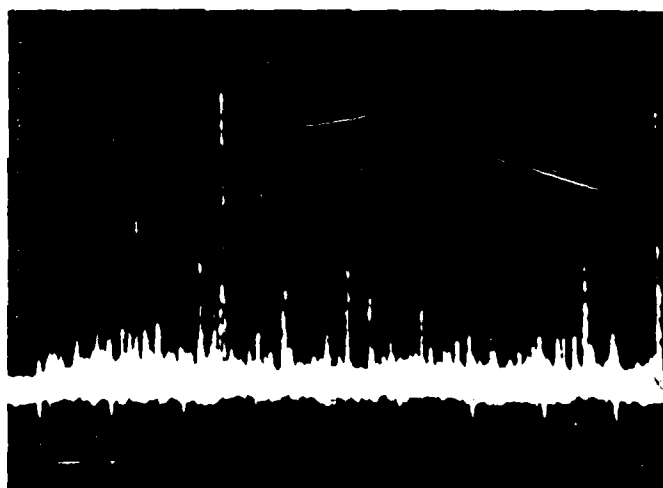


Figure 40. Oscillograph of Pulses Resulting
from Laser Light-Scattering System

shown in Figure 40. For a more detailed description of the ARL/PSU laser light-scattering system and Mie scattering theory, see Reference 28.

The pulse-height analyzer was designed and built at ARL/PSU. A threshold could be set such that no pulses below a specified voltage would be counted by the analyzer. Using a sequence of equally spaced internal reference voltages, the analyzer possessed sixteen storage areas where the incoming pulses were sorted out according to their height. The sixteenth category was open-ended and accepted any pulse above a certain voltage. Upon starting the operation of the analyzer, incoming pulses were continuously categorized and counted until some predetermined total number was reached. At that point, the analyzer displayed the time of operation and the number of pulses in each of the sixteen categories.

Assuming cavitation nuclei to be the only objects scattering light, and furthermore, that they are roughly spherical, the Mie scattering theory could then be used with the pulse height distribution to determine the size distribution of the cavitation nuclei. Information of the total counting time and the size of the control volume through which the particles were counted would determine the density of nuclei in the tunnel. Most remarkably, all of this information is gathered in a matter of seconds. This is a vast improvement over other systems used to count nuclei, notably holographic systems which, although quick to acquire the data, require extensive periods of time for people to visually count all of the nuclei. Thus, the laser light-scattering system has the advantage of being virtually on-line.

Preliminary tests using the system proved to be highly disappointing with its erratic results. While running the tunnel under virtually identical conditions, vastly different counting times were often recorded. On the other hand, varying the pressure at one particular velocity would be expected to alter the size distribution of the nuclei, but this was not observed to any significant degree. Finally, spherical particles of known diameter that reflected light in water much like a bubble were used to seed the tunnel. Increasing the concentration tended to produce the correct size distribution for the particles as well as being counted more quickly by the analyzer.

The conclusion drawn from these results was that, although the system was functioning correctly, dirt particles were making a major contribution to the scattering process. This matter is the subject of an investigation currently underway at ARL/PSU. It was unfortunate that the scattering system was not able to complement this particular study.

DISTRIBUTION LIST FOR ARL UNCLASSIFIED TM No. 81-76 by M. F. Hamilton,
dated 2 March 1981

Commander
Naval Sea Systems Command
Department of the Navy
Washington, DC 20362
Attn: S. M. Blazek
Code NSEA-05HB
(Copy No. 1)

Naval Sea Systems Command
Attn: H. C. Claybourne
Code NSEA-05H5
(Copy No. 2)

Naval Sea Systems Command
Attn: J. H. Huth
Code NSEA-05DC2
(Copy No. 3)

Naval Sea Systems Command
Attn: F. E. Eissing
Code NSEA-05H
(Copy No. 4)

Naval Sea Systems Command
Attn: E. G. Liszka
Code NSEA-63R1
(Copy No. 5)

Naval Sea Systems Command
Attn: T. E. Peirce
Code NSEA-63R3
(Copy No. 6)

Naval Sea Systems Command
Attn: A. R. Paladino
Code NSEA-05H1
(Copy No. 7)

Naval Sea Systems Command
Attn: F. Romano
Code NSEA-05R
(Copy No. 8)

Commanding Officer
Naval Underwater Systems Center
Newport, RI 02840
Attn: D. Goodrich
Code 3634
(Copy No. 9)

Naval Underwater Systems Center
Attn: T. A. Davis
Code 36314
(Copy No. 10)

Naval Underwater Systems Center
Attn: R. J. Kittredge
Code 3634
(Copy No. 11)

Naval Underwater Systems Center
Attn: R. Trainor
Code 36314
(Copy No. 12)

Naval Underwater Systems Center
Attn: P. Corriveau
(Copy No. 13)

Commanding Officer
Naval Ocean Systems Center
San Diego, CA 92152
Attn: D. Nelson
Code 6342
(Copy No. 14)

Commander
David W. Taylor Naval Ship R&D Center
Department of the Navy
Bethesda, MD 20084
Attn: W. K. Blake
Code 1905
(Copy No. 15)

David W. Taylor Naval Ship R&D Center
Attn: T. E. Brockett
Code 1544
(Copy No. 16)

David W. Taylor Naval Ship R&D Center
Attn: R. W. Brown
Code 1942
(Copy No. 17)

David W. Taylor Naval Ship R&D Center
Attn: R. A. Cumming
Code 1544
(Copy No. 18)

David W. Taylor Naval Ship R&D Center
Attn: T. M. Farabee
Code 1942
(Copy No. 19)

David W. Taylor Naval Ship R&D Center
Attn: F. E. Geib
Code 1942
(Copy No. 20)

DISTRIBUTION LIST FOR ARL UNCLASSIFIED TM No. 81-76 by M. F. Hamilton,
dated 2 March 1981

David W. Taylor Naval Ship R&D Center
Attn: J. H. McCarthy
Code 154
(Copy No. 21)

David W. Taylor Naval Ship R&D Center
Attn: T. C. Mathews
Code 1942
(Copy No. 22)

David W. Taylor Naval Ship R&D Center
Attn: W. B. Morgan
Code 15
(Copy No. 23)

David W. Taylor Naval Ship R&D Center
Attn: K. D. Remmers
Code 1942
(Copy No. 24)

David W. Taylor Naval Ship R&D Center
Attn: M. M. Sevik
Code 19
(Copy No. 25)

David W. Taylor Naval Ship R&D Center
Attn: J. Shen
Code 194
(Copy No. 26)

Commander
Naval Surface Weapons Center
Silver Spring, MD 20910
Attn: G. C. Gaunard
Code R-31
(Copy No. 27)

Office of Naval Research
Department of the Navy
800 N. Quincy Street
Arlington, VA 22217
Attn: M. M. Reischmann
(Copy No. 28)

Office of Naval Research
Attn: H. Fitzpatrick
Code 438
(Copy No. 29)

Defense Technical Information Center
5010 Duke Street
Cameron Station
Alexandria, VA 22314
(Copy Nos. 30 to 35)

Dr. Bruce D. Cox
Hydrodynamics Research Assoc., Inc.
7900 Inverness Ridge Road
Potomac, MD 20954
(Copy No. 36)

Allis-Chalmers Corp.
Hydro-Turbine Division
Box 712
York, PA 17405
Attn: R. K. Fisher
(Copy No. 37)

Rand Corporation
1700 Main Street
Santa Monica, CA 90406
Attn: C. Gazley
(Copy No. 38)

Netherlands Ship Model Basin
Haagsteeg 2
P.O. Box 28
67 AA Wageningen
The Netherlands
Attn: Mr. J. van der Kooij
(Copy No. 39)

Netherlands Ship Model Basin
Attn: Dr. J. van der Meulen
(Copy No. 40)

Netherlands Ship Model Basin
Attn: G. Kuiper
(Copy No. 41)

Dr. rer. nat. Horst Merbt
Forschungsbeauftragter für Hydroakustik
8012 Ottobrunn B Munchen
Waldparkstr. 41
Munich
Germany
(Copy No. 42)

Mr. H. J. Baiter
Fraunhofer-Institut für Hydroakustik
Postfach 260
8012 Ottobrunn
Fed. Rep. of Germany
(Copy No. 43)

Dr. Ir. A. De. Bruijn
Technisch Physische Dienst TNO-TH
Stieltjesweg 1
Postbus 155
Delft
The Netherlands
(Copy No. 44)

DISTRIBUTION LIST FOR ARL UNCLASSIFIED TM No. 81-76 by M. F. Hamilton,
dated 2 March 1981

Dr. Allen Moore
Admiralty Research Laboratory
Teddington, Middlesex
England
(Copy No. 45)

Dr. Wittendorf
HSVA
Hamburg
Germany
(Copy No. 46)

Von Karman Inst. for Fluid Dynamics
Turbomachinery Laboratory
Rhode-Saint-Genese
Belgium
Attn: Library
(Copy No. 47)

Dr. V. H. Arakeri
Department of Mechanical Engineering
Indian Institute of Science
Bangalore 560 012
India
(Copy No. 48)

Institute of High Speed Mechanics
Tohoku Univeristy
Sendai
Japan
(Copy No. 49)

Dr. Allan J. Acosta
California Institute of Technology
Division of Engineering for
Applied Sciences
Pasadena, CA 91109
(Copy No. 50)

Dynamics Technology, Inc.
3838 Carson Street, Suite 110
Torrance, CA 90503
Attn: Wayne H. Haigh
(Copy No. 51)

Bolt, Beranek and Newman
50 Moulton Street
Cambridge, MA 02136
Attn: Dr. N. A. Brown
(Copy No. 52)

Bolt, Beranek and Newman
Attn: D. Chase
(Copy No. 53)

Bolt, Beranek and Newman
Attn: K. L. Chandiramani
(Copy No. 54)

Prof. Patrick Leehey
Dept. of Ocean Engineering - Room 5-222
Massachusetts Institute of Technology
77 Massachusetts Avenue
Cambridge, MA 02139
(Copy No. 55)

Naval Postgraduate School
The Presidio
Monterey, CA 93940
Attn: Library
(Copy No. 56)

Dr. Roger E. A. Arndt
St. Anthony Falls Hydraulic Laboratory
University of Minnesota
Mississippi River at 3rd Ave., S.E.
Minneapolis, MN 55414
(Copy No. 57)

Defense Advanced Research Projects Agency
1400 Wilson Boulevard
Arlington, VA 22209
Attn: P. Selwyn, TPO
(Copy No. 58)

Creare, Inc.
Box 71
Hanover, NH 03755
Attn: W. Swift
(Copy No. 59)

Hydronautics, Inc.
Pindell School Road
Laurel, MD 20810
(Copy No. 60)

Dr. J. W. Hoyt
Rutgers University
College of Engineering, Industrial
and Aerospace Engineering
P.O. Box 909
Piscataway, NJ 08854
(Copy No. 61)

DISTRIBUTION LIST FOR ARL UNCLASSIFIED TM No. 81-76 by M. F. Hamilton,
dated 2 March 1981.

Applied Research Laboratory
The Pennsylvania State University
Post Office Box 30
State College, PA 16801
Attn: R. E. Henderson
(Copy No. 62)

Applied Research Laboratory
Attn: G. C. Lauchle
(Copy No. 63)

Applied Research Laboratory
Attn: D. E. Thompson
(Copy No. 64)

Applied Research Laboratory
Attn: E. G. Taschuk
(Copy No. 65)

Applied Research Laboratory
Attn: J. W. Holl
(Copy No. 66)

Applied Research Laboratory
Attn: M. L. Billet
(Copy No. 67)

Applied Research Laboratory
Attn: D. R. Stinebring
(Copy No. 68)

Applied Research Laboratory
Attn: R. S. Moyer
(Copy No. 69)

**DAI
FILM**